Unraveling the transformation of void and strain localization induced ductile damage based on the deformation heterogeneity affected by size and hardening effects

Xiaoqing Shang[1], M.W. Fu[2], Haiming Zhang[3], Juan Liu[3], Xiao Zhou[4], Tao Ying[1], Wenjiang Ding[1,4], Xiaoqin Zeng[1,4] *

[1] *National Engineering Research Center of Light Alloy Net Forming, School of Materials Science and Engineering, Shanghai Jiao Tong University, Shanghai 200240, China*
[2] *Department of Mechanical Engineering, Research Institute for Advanced Manufacturing, The Hong Kong Polytechnic University, Hung Hom, Kowloon, Hong Kong*
[3] *Institute of Forming Technology & Equipment, School of Materials Science and Engineering, Shanghai Jiao Tong University, Shanghai 200030, China*
[4] *State Key Laboratory of Metal Matrix Composites, Shanghai Jiao Tong University, Shanghai 200240, China*

Abstract

This study delves into the ductile damage mechanism via exploring the intrinsic nature of the change of damage mechanism and behaviors based on the deformation heterogeneity, which is affected by the effect of the grain and geometrical sizes and the hardening of polycrystalline metals. In tandem with this goal, tensile experiments using ductile metals of pure titanium and austenite steel with different grain sizes ($\bar{d}$) and sample thicknesses (t) were conducted to obtain various damage behaviors. The damage mechanism featured with large amounts of voids and deep dimples is defined as void damage (D_v); while the void-suppressed damage characterized by flat fracture surfaces is termed as strain localization induced damage (D_l). Examinations of damage characteristics show that the increase of $t/\bar{d}$ or the increase of hardening brings about the transformation of D_l to D_v. This damage behavior is correlated to the deformation characterized by heterogeneity. Crystal plasticity finite element simulation considering the high-fidelity microstructures was conducted to reveal the grain-level deformation heterogeneities. Both the results about size and hardening effects support an observed phenomenon that severer inhomogeneous deformation is accompanied with fewer voids; while a more uniform deformation induces obvious void growth. The deformation

heterogeneity is thus identified to be a crucial factor which affect the transformation of D_l and D_v. The intrinsic nature of this transformation roots in the pattern of energy dissipation. Plastic deformation which generates a larger continuous strain localization zone is favorable for the formation of grain/subgrain boundaries. As the energy is consumed by the formation of grain boundaries, void nucleation and growth become difficult. To relate the damage mode to strain distribution pattern, a characteristic parameter representing the change of D_l and D_v is introduced and defined. The proposed intrinsic relationship between damage mechanism and deformation heterogeneity, and the characteristic parameter is articulated by a D_l - D_v paradigm developed in this research. This paradigm can be used to predict and interpret the damage performance of various metallic materials, and it shows a wide applicability and predictive ability. The explorations are expected to add new horizons to the understanding of damage mechanism and to support the development of damage free products.

Keywords: Ductile damage; Void; Heterogeneous deformation; Energy dissipation; Crystal plasticity.

Corresponding author:

* Xiaoqin Zeng; E-mail: xqzeng@sjtu.edu.cn

1. Introduction

Ductile metals fail in two ways: void and strain localization induced fracture (Pineau et al., 2016). During plastic deformation, internal voids evolve through nucleation, growth and coalescence, inducing an increase of void number, size, and fraction (Kondori et al., 2018; Ueda et al., 2014). Void damage (D_v) denotes the mechanism that the internal voids play a dominant role in the final failure. Representative features of D_v involve larger voids inside materials and a number of deep dimples at the fracture surface (Besson, 2009; Li et al., 2011; Taylor and Sherry, 2012). Another type of ductile fracture refers to a void-suppressed mechanism, which is generally termed as 'void sheeting' (Azghandi et al., 2020; Besson, 2009; Roth et al., 2018; Ueda et al., 2014). It articulates the damage behavior featured with fewer voids and a flat fracture surface. An explanation for the mechanism is that many smaller secondary voids nucleate and coalesce in the strain localization bands (Bandstra et al., 1998; Besson, 2009; Kadkhodapour et al., 2011; Tvergaard, 1982; Xue, 2008). This description and the results of this study both support a point that strain localization plays a key role in the void-suppressed failure, and thus this mechanism is defined as strain localization induced damage (D_l). By using necking as an instance, it is an illustration of strain localization. The mechanisms of D_v and D_l are interpreted in the schematic in Fig. 1.

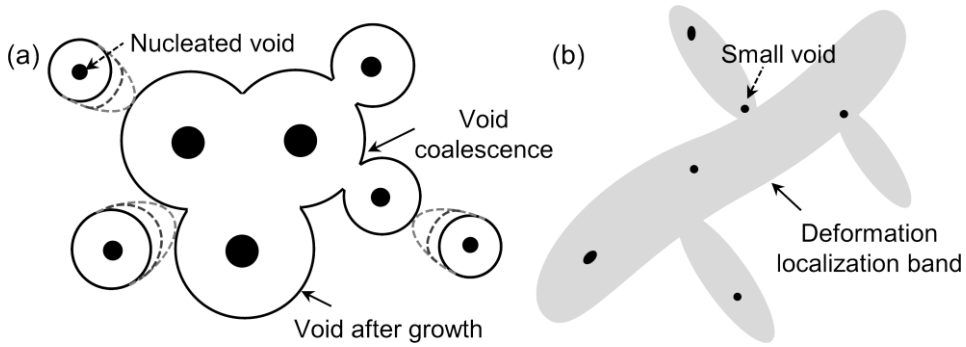

Fig. 1. Ductile damage mechanism of (a) void damage, and (b) strain localization induced damage.

Grain and geometrical size affect the ductile damage mechanism of polycrystalline metal. As reported by Meng and Fu (2015), Xu et al., (2015), and Furukimi et al. (2017), the number of

nucleated voids in pure copper increase with the increase of $t/\bar{d}$ (t denotes the thickness and $\bar{d}$ the average e grain size). Meanwhile, the fracture mode transforms from a void-suppressed mode to a void-dominated one as $t/\bar{d}$ increases from 1 to 10. Similar law also shows for high-purity iron (Furukimi et al., 2017) and stainless steel (Shang et al., 2020): the increase of t or the decrease of $\bar{d}$ induces an increase of the number and volume fraction of voids. Xu et al. (2015) interpreted this size effect by considering that the interior of a sample is more prone to void formation than the free surface. However, as stated by Zhang et al. (2018), the grain boundary triple junctions at the free surface bring about strain and stress concentrating and trigger through-thickness shear bands in samples with a smaller $t/\bar{d}$. Therefore, free surface is the primary micro-crack initiation site in the smaller $t/\bar{d}$ scenario. The different points referring damage initiation region indicate unclearness about the size effect of ductile damage mechanism. Especially, some issues of the void-suppressed fracture remain elusive. Tradition theories refer D_l as coalescence of 'secondary void' (Bandstra et al., 1998; Besson, 2009); however, there is not a specific definition or much experimental evidence for the so-called 'secondary void'.

An alternative perspective for interpreting the size effect of ductile damage is the deformation characteristics. With a careful examination of the plentiful size effect studies, a common law about the relation between size and surface roughening is obtained: the free surface roughening is promoted with the decrease of $t/\bar{d}$ ratio, leading to nonuniformity of the sample thickness; as $t/\bar{d}$ increases, the free surface fluctuation becomes moderate (Furukimi et al. 2014; Meng and Fu, 2015; Furukimi et al., 2017; Xu et al., 2015; Fu and Wang, 2021). Quantitative analysis of the surface fluctuation shows an increase of the normalized sample height from 0.0126 to 0.0755 as $t/\bar{d}$ is decreased from 10 to 1.5. Since free surface roughening is an outcome of plastic deformation, it is believed that delving the relationship between damage and deformation helps unravel the transformation mechanism of D_v and D_l with grain and geometrical size.

Work hardening is another factor that greatly affect the ductility of metallic materials. There is a consensus that the increase of hardening relieves strain localization, delays necking, and helps improve ductility (Shao et al., 2018; Wu and Fan, 2020). A lot of efforts have been devoted into exploring the hardening mechanism in terms of precipitations (Chen et al. 2015; Yang et al., 2018), hierarchically heterogeneous microstructure (Wang et al., 2018; Wu et al., 2017; Wu et al., 2015), and the dislocation motion (Cheng et al., 2018; Shao et al., 2018; Yang et al., 2020). However, critical issues of the damage mechanism change with work hardening have not raised much concern. In tandem with this, the fracture features of metals with different hardening properties were carefully examined to give a damage panorama. In uniaxial tension deformation of high-hardening materials, such as stainless steels (Shang et al., 2020), and aluminum alloys (Li et al., 2011; Pedersen et al., 2015), D_v dominates the failure with fracture featuring larger voids and large dimples; while the low-hardening materials, such as pure titanium (Daming et al., 2017; Sun et al., 2021; Wang et al., 2018), pure tantalum (Noell et al., 2017), and dual-phase steel (Li et al., 2020; Park et al., 2014; Zhao et al., 2014) are apt to a D_l mode with distinct features of shallow dimples and a relatively flat fracture. A transformation of D_l and D_v induced by the change of hardening is thus identified. A critical step for uncovering the hardening affected damage mechanism is to figure out the change of strain localization, D_l and D_v contributions with the change of work hardening.

Emphasis is also placed on the micro-mechanism of the D_v and D_l transformation. Void is a kind of bulk defect in materials that forms with the aggregation of smaller defects of dislocations and vacancies (Noell et al., 2017; Noell et al., 2020; Ungár et al., 2007; ZEHETBAUER et al., 2006; Nguyen and Warner, 2017). Plentiful void damage researches denote that voids with dimensions ranging from several microns to tens of microns play a dominant role in the ductility (Azghandi et al., 2020; Kondori et al., 2018; Taylor and Sherry, 2012; Ueda et al., 2014). A fact has been neglected in the ductile damage arena is that void is not the sole defect form at the mesoscale. The boundary defect, involving grain boundary, twin

boundary is another manifestation. As is well known, the inherent plastic deformation inhomogeneity at the grain-scale induces an increase of grain boundary (GB) area. For a cube-shaped grain, the grain surface area is increased by 16% with 50% rolling reduction; it is increased by 3267% after 99% rolling reduction (Humphreys and Hatherly, 2012). A study about the subgrain structure reports a dislocation density increase and substructure formation during cold rolling of a commercial-purity titanium. With the applied strain of 0.5, the area fraction of high-angle grain boundary increases from 13.6% to 66.1%, and the grain size is reduced from 14.4 to 1.6 μm (Zherebtsov et al., 2011). Physically, plastic deformation is derived from the breading and re-establishment of atom bonds; various kinds of defects generate during the process. Therefore, damage accumulation is a concomitant of plastic deformation, and the deformation characteristic is an intrinsic factor to defect and damage. Delving deeper into the intrinsic nature of the non-uniform deformation dominated defect mechanism is supposed to add new horizons to the understanding of ductile damage.

The understanding of damage mechanisms determines the methodology of damage modeling. Until now, various models have been established to articulate the damage accumulation of metal aggregates (Boyce et al., 2016; Boyce et al., 2014; Li et al., 2011). For copper, iron, steels (Johnson and Cook, 1985; Shang et al., 2017), aluminum alloys 6082 (Lou et al., 2017), 6061 (Li et al., 2011) and 2024 (Bai and Wierzbicki, 2008), magnesium alloy ZEK100 (Habib et al., 2019), specific formulations have been developed based on the influence of stress state. Considering that ductile damage is susceptible to material, size, and microstructure, a new model has to be constructed when those factors change. Correspondingly, new experiments have to be conducted to calibrate material parameters in the model. This is definitely a time-consuming and low-fidelity process, inducing great complexity in the arena of ductile damage modeling. Searching for a unified modeling methodology is thus of great importance. In tandem with this, figuring out a general relation between damage and deformation, and defining a parameter to represent the relation are necessities.

This study provides an in-depth elaboration on the relation between damage behaviors and deformation characteristics by employing a combined experiment and simulation approach. Firstly, experiments were conducted for representative ductile metals with various grain and sample sizes to obtain different damage behaviors, involving the ones featured with D_v, D_l, and a mixed mode. Through careful characterization and analysis of the damage and deformation characteristics, the deformation heterogeneity is determined as the crucial factor affecting the damage behavior. Moreover, the way that non-uniform deformation influences ductile damage is revealed based on microstructure examination and high-fidelity simulation. Via relating the strain distribution pattern and the damage feature, a characteristic parameter representing the transformation of D_v and D_l is defined. Applicability of the developed D_l - D_v paradigm is analyzed by comparing the predicted and experimental damage behavior changes with hardening, size, and second phase. For different metal polycrystals, a good agreement is achieved between the predicted damage characteristics and experimental observations.

2. Experiment and CPFEM modeling methodology

2.1 Material and experiment design

Pure titanium and austenite steel which feature typical ductile fractures were used for the damage mechanism investigation. The as-received pure titanium was a rolled sheet. It was annealed at 500℃ for 1 hour to obtain equiaxed grain with grain size ($\bar{d}$) of 20 μm [Fig. 2(a)], and at 750 for 1 hour to get $\bar{d}$ of 120 μm [Fig. 2(b)]. As for the austenite steel, the hot forged materials with $\bar{d}$ of 20 μm [Fig. 2(c)] and 120 μm [Fig. 2(d)] were employed for testing. Uniaxial tensile experiment was conducted for two types of samples, which are termed No. 1 and No. 2 [Fig. 2(e)]. The tested samples have a small gauge region on account of high-resolution digital image correlation (DIC) measurement and micro-computed tomography (XCT) test. To study the size effect of ductile damage, tailor-designed experiments with different values of $t/\bar{d}$ were performed. Table 1 lists the $\bar{d}$, sample type, t and $t/\bar{d}$ of all the designed experiments. For pure titanium, three $t/\bar{d}$ conditions were considered, i.e., $t/\bar{d}$=10, 60 and 100; for austenite steel, the deformation and damage of samples with of $t/\bar{d}$=7.5, 10,

60 were studied.

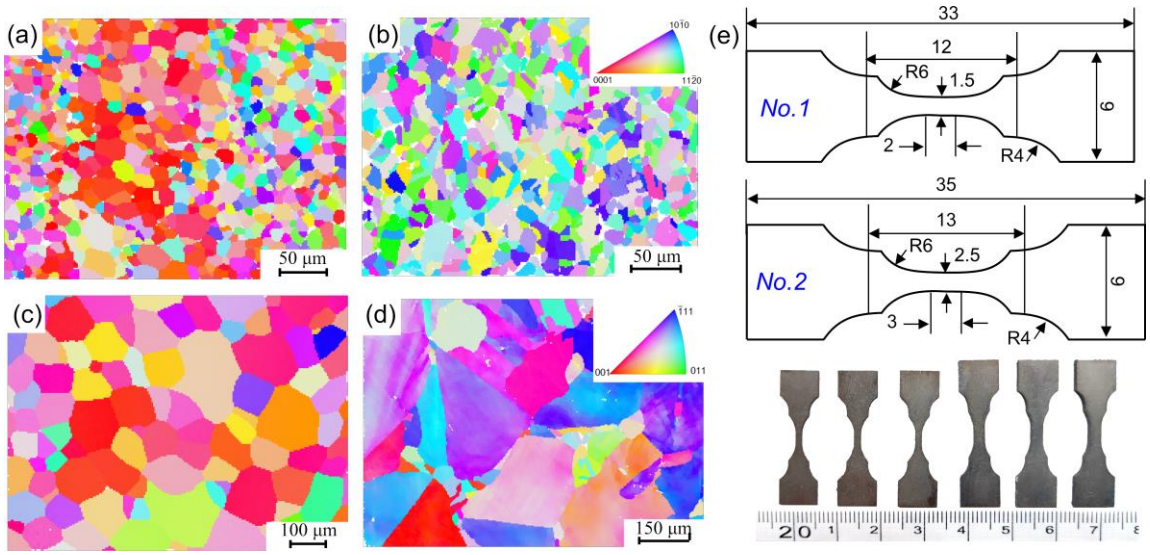

Fig. 2. Microstructure and the tested samples: Electron backscatter diffraction (EBSD) results for pure titanium with (a) $\bar{d}$ =20 μm, and (b) $\bar{d}$ =120 μm. Stainless steel 316LN with mono-austenite phase and (c) $\bar{d}$ =20 μm, and (d) $\bar{d}$ =120 μm. (e) Sample shape and dimension.

Table 1 Experiment design for the two tested materials

Pure titanium			**Austenite steel**		
Grain size ($\overline{d, mm}$)	Specimen	$t/\bar{d}$	Grain size ($\overline{d\ mm}$)	Specimen	$t/\bar{d}$
120	No.1, t=1.2	10	120	No.1, t =0.9	7.5
20	No.1, t =1.2	60	120	No.1, t =1.2	10
20	No.2, t =2.0	100	20	No.1, t =1.2	60

Fracture characteristics were examined by the micro-computed tomography (XCT). XCT is a non-destructive technique for three-dimensional visualization and quantitative analysis of internal voids. It recognizes void via its gray level variation with the matrix material. The results of XCT also present the morphology of the free surface, which is an indicator of deformation heterogeneity. The XCT technology has been widely employed in the study of damage mechanism in terms of the void evolution, the relation between damage and

microstructure, and the critical fracture condition (Azghandi et al., 2020; Kondori et al., 2018; Taylor and Sherry, 2012; Ueda et al., 2014). This study adopted XCT to identify the variation of the internal voids and the free surface morphology in different size and the hardening scenarios. Voxel resolution employed in XCT examinations was 1.0 μm. Concerning that a detectable damage feature had three voxels in each direction, the voids with volume larger than 27 x $(1.0\ \mu m)^3$=27 μm^3 were recognized. Every XCT result involves a thousand two-dimensional slices, and the three-dimensional solid is re-constructed from the slices. Fig. 3 displays representative solid reconstruction and two-dimensional slices for the parent pure titanium and austenite steel. The results show that there are few initial voids in the as-received metals.

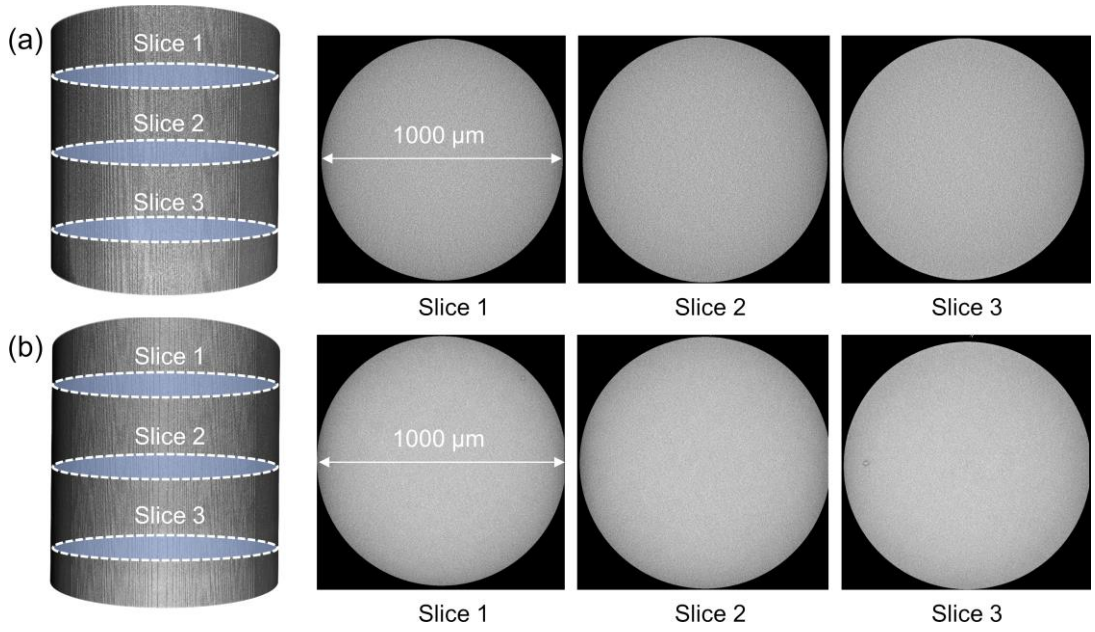

Fig. 3. XCT examination for initial voids in the as-received materials: (a) pure titanium, and (b) stainless steel 316LN.

The strain distribution and evolution were measured by the digital image correlation (DIC) technic. The testing equipment is an assembly of a load cell with loading capacity of 5000N and a microscope. Speckles were made on the surface of the samples and strains were computed based on the speckle morphology before and after plastic deformation. The main purpose of

conducting DIC measurements was to provide experimental corroborations of the simulated strain results. Representative results of tensile experiment employing the DIC technic for pure titanium and austenite steel are present in Fig. 4. Damage feature examinations of XCT were performed at pre-fracture stage of uniaxial tension when an obvious load drop occurs; the examination point is marked in the load-stroke curve in Fig. 4. The region for XCT characterization is the localized deformation area featured by obvious section area reduction. Fig. 5 displays two-dimensional slices for all the studied damage scenarios in the pre- fracture situation. From the results, the internal voids and necking behavior are clearly recognized.

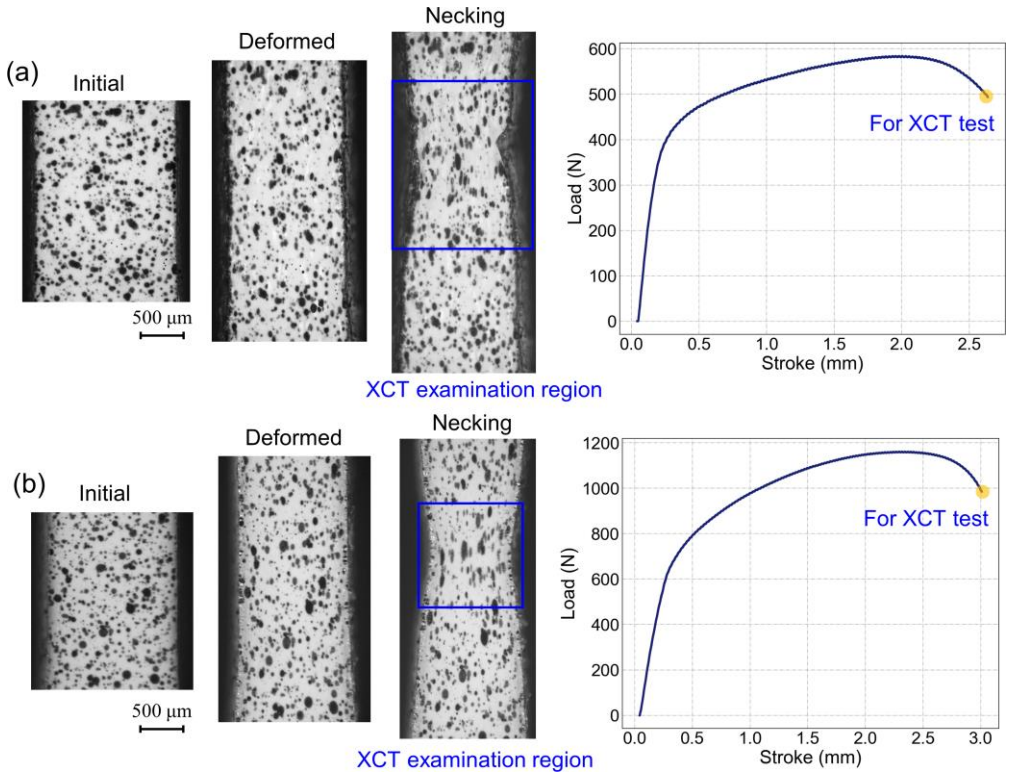

Fig. 4. Representatives of tensile experiment employing the DIC technic. Speckle on surface of samples and its evolution during tensile loading, and the load-stroke curve for (a) pure titanium with $\bar{d}$ =20 μm, and (b) austenite steel 316LN with $\bar{d}$ =120 μm.

2.2 Crystal plasticity finite element modeling

The mesoscale deformation features were studied by the full-field crystal plasticity finite element modeling (CPFEM). CPFEM is adept at articulating the grain-scale mechanical responses, involving heterogeneous deformation, grain orientation evolution, slip and twinning

behaviors (Roters et al., 2019; Zhang et al., 2016; Shang et al., 2021). Compared with the traditional mean-field CP-based method, full-field CP modeling has merits of representing real grain morphology, local grain interaction, and the intra-grain deformation heterogeneity. CPFEM is suitable for studying damage mechanism as it represents the deformation characteristics at the same length scale as void. Selvarajou et al. (2019) investigated the crystallographic aspect of void growth and coalescence by conducting CPFEM simulation with prefabricate voids, and identified the effects of orientation and extension-twinning induced reorientation on void evolution. Through carrying out CPFEM simulations for RVE with high-fidelity microstructure and initial voids, Shang et al. (2020) discovered a Gaussian distribution of void size and developed a void model; the model represents the influence of grain size and the variation of void size in materials.

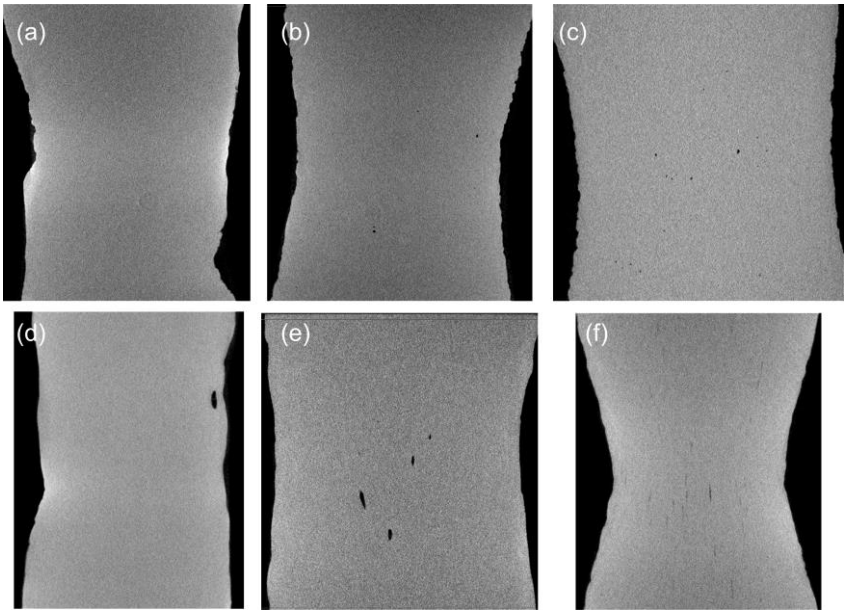

Fig. 5. Two-dimensional slices from XCT examinations at pre-fracture stage showing localized necking and internal voids for pure titanium with (a) $t/\bar{d}$ =10, (b) $t/\bar{d}$ =60, (c) $t/\bar{d}$ =100, and austenite steel 316LN with (d) $t/\bar{d}$ =7.5, (e) $t/\bar{d}$ =10, (f) $t/\bar{d}$ =60.

The CPFEM model adopted in the study described anisotropic elastic behavior of crystals by a generalized Hook's law (Roters et al., 2019). For the modeling of dislocation slip and twinning behaviors, a rate-dependent power-law equation was utilized (Salem et al., 2005). The plastic

velocity gradient is denoted as the following:

$$\mathbf{L}_0^{\mathrm{p}} = (1.0 - f_{\mathrm{tw}}) \sum \dot{\gamma}_{\mathrm{sl}}^{\alpha} \mathbf{S}_{\mathrm{sl}}^{\alpha} + f_{\mathrm{tw}} \sum \dot{\gamma}_{\mathrm{tw}}^{\beta} \mathbf{S}_{\mathrm{tw}}^{\beta} + f_{\mathrm{tw}} \sum \dot{\gamma}_{\mathrm{sl}}^{\alpha} \hat{\mathbf{S}}_{\mathrm{sl}}^{\alpha} \quad (1)$$

where $\mathbf{S}_{\mathrm{sl}}^{\alpha}$, $\hat{\mathbf{S}}_{\mathrm{sl}}^{\alpha}$, $\mathbf{S}_{\mathrm{tw}}^{\beta}$ are the Schmid tensors of slips in the untwinned matrix, twinned matrix, and the twinning systems. $\dot{\gamma}_{\mathrm{sl}}^{\alpha}$ and $\dot{\gamma}_{\mathrm{tw}}^{\beta}$ denote the plastic shearing rates of the α-th slip system and the β-th twinning system. f_{tw} is the volume fraction of twinning.

The shearing rate is formulated with power-law expressions as:

$$\dot{\gamma}_{\mathrm{sl}}^{\alpha} = \dot{\gamma}_{\mathrm{sl}}^{0} \left| \frac{\tau_{\mathrm{sl}}^{\alpha}}{g_{\mathrm{sl}}^{\alpha}} \right|^{1/\mathrm{m_{sl}}} \mathrm{sign}(\tau_{\mathrm{sl}}^{\alpha}), \text{ and } \dot{\gamma}_{\mathrm{tw}}^{\beta} = \dot{\gamma}_{\mathrm{tw}}^{0} \langle \frac{\tau_{\mathrm{tw}}^{\beta}}{g_{\mathrm{tw}}^{\beta}} \rangle^{1/\mathrm{m_{tw}}} \quad (2)$$

where $\dot{\gamma}_{\mathrm{sl}}^{0}$ and $\dot{\gamma}_{\mathrm{tw}}^{0}$ are the reference shear rate. $\mathrm{m_{sl}}$ and $\mathrm{m_{tw}}$ are the rate sensitivity parameter. The slip and twinning resistance of g_{sl}^{α} and g_{tw}^{β} are articulated as:

$$\dot{g}_{\mathrm{sl}}^{\alpha} = h_{\mathrm{sl}}^{0}(1 + c_1 \cdot f_{\mathrm{tw}}) \sum_{\xi} \left(1 - \frac{g_{\mathrm{sl}}^{\xi}}{g_{\mathrm{sl}}^{\infty}}\right)^{n} \dot{\gamma}_{\mathrm{sl}}^{\xi} \quad (3)$$

$$\dot{g}_{\mathrm{tw}}^{\beta} = h_{\mathrm{tw}}^{0}(f_{\mathrm{tw}})^{c_2} \sum_{\zeta} \dot{\gamma}_{\mathrm{tw}}^{\zeta} + h_{\mathrm{tw-sl}}^{0} (\sum_{\alpha} \gamma_{\mathrm{sl}}^{\alpha})^{c_3} \sum_{\xi} \dot{\gamma}_{\mathrm{sl}}^{\xi} \quad (4)$$

where h_{sl}^{0}, h_{tw}^{0} and $h_{\mathrm{tw-sl}}^{0}$ are the initial slip hardening modulus, initial twin hardening moduli caused by the interactions of twin-twin and slip-twin. g_{sl}^{∞} is the saturated value of slip resistance.

Both two-dimensional (2D) and three-dimensional (3D) CPFEM simulations were conducted to study the deformation characteristics. 2D simulation was performed to get a high-resolution strain map. Based on this data, the influences of size and hardening on the plastic deformation pattern were carefully analyzed. The 2D CPFEM modeling of representative volume elements (RVEs) with different values of $t/\bar{d}$ is shown in Fig. 6. Grains in the RVE were assigned as random orientations. A uniaxial tension boundary condition with a far-field true strain (ε_{ff}) of 0.4 is imposed. $\varepsilon_{ff} = 0.4$ denotes a pre-fracture deformation state for the high-ductility pure titanium and austenite steel. For the two boundaries at the thickness direction, one was imposed a symmetry boundary condition and the other was a free surface. By using this boundary condition, the fluctuation of free surface revealed by XCT examination can be reproduced by

simulation. For each studied scenario, three groups of simulations were conducted via changing grain orientations.

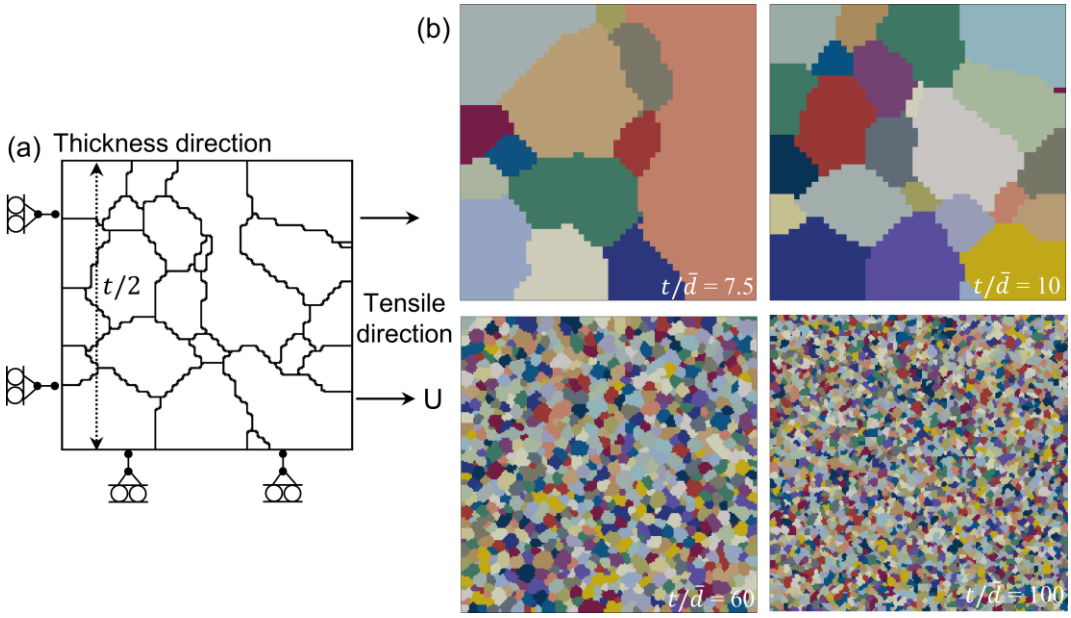

Fig. 6. 2D CPFEM modeling for high-resolution results: (a) boundary condition, and (b) scenarios with different ratios of $t/\bar{d}$.

3D CPFEM model for the tested plate sample was established [Fig. 7(a)]. Symmetry condition was imposed on the tensile, width and thickness directions, and the model represents 1/8 of the sample. Due to the computational limit, 3D simulation was only performed for the scenario with fewer grains at the thickness. The 3D simulations represent the deformation characteristics of the real sample, and quantitative analysis was done in accordance with the results. Material parameters adopted for the CPFEM simulation are listed in Table 2. The parameters were determined based on previously reported data (Shang et al., 2020; Yang et al., 2011), and the comparisons between experimental and simulated results. Fig. 7(b) presents a good agreement of stress-strain relation obtained by uniaxial tensile tests and simulations for pure titanium and austenite steel.

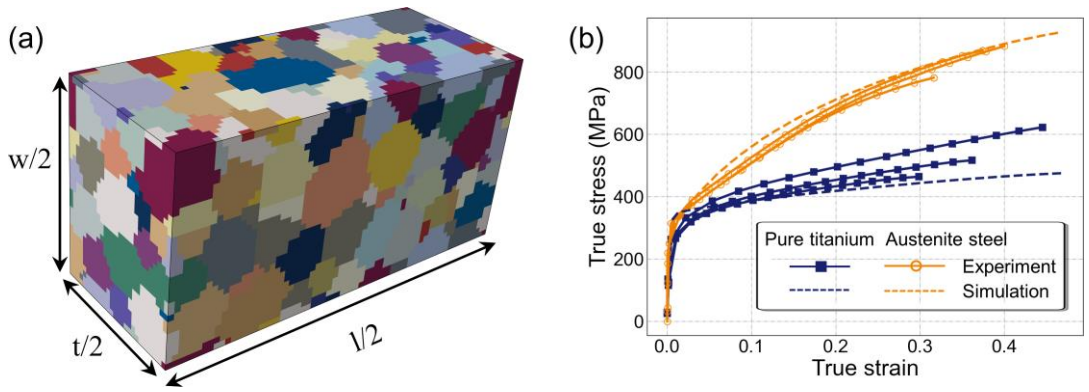

Fig. 7. Sample-scale 3D CPFEM modeling for quantitative analysis. (a) Three-dimension CPFEM modeling for $t/\bar{d}$ =10. Symmetry is considered and the model represents 1/8 of the tested plate sample. (b) Comparison of the experimental and simulated strain-stress curves. For each condition, three parallel tensile experiments were performed, and the simulations with three groups of different grain orientations were conducted.

Table 2 Material parameters for CPFEM simulation

Stainless steel 316LN					
Elastic properties (GPa)	C_{11}		C_{12}		C_{44}
	262.5		112.5		75.0
Plastic properties					
Slip system	{hkl} <uvw>	g_0 (MPa)	g_s (MPa)	h_0 (MPa)	a
	$\{111\}\langle 1\bar{1}0\rangle$	95.0	395.0	1050.0	2.5
Pure Ti					
Elastic properties (GPa)	C_{11}	C_{12}	C_{13}	C_{33}	C_{44}
	163.0	114.0	69.3	191.0	38.0
Plastic properties					
Slip system	<uvtw>	g_0 (MPa)	g_s (MPa)	h_0 (MPa)	a
Basal	$\{0001\}\langle 11\bar{2}0\rangle$	130.0	350.0	340.0	2.0
Prismatic	$\{10\bar{1}0\}\langle 11\bar{2}0\rangle$	70.0	220.0	250.0	2.0
Pyramidal <c+a>	$\{10\bar{1}1\}\langle 11\bar{2}3\rangle$	180.0	500.0	400.0	2.0
Twin	$\{10\bar{1}2\}\langle 10\bar{1}1\rangle$	250.0	/	/	/

3. Results and discussions

3.1 Transformation of void and strain localization induced ductile damage

The damage features, involving the internal voids, fluctuations of free surface, and the fractography were carefully examined and shown in Figs. 7-8. The contribution of voids is measured by a widely used parameter void volume fraction (f), and the values of f for the studied damage cases are listed in Table 3. A great variation of damage behaviors with materials and $t/\bar{d}$ is shown. Void damage is greatly suppressed in pure titanium with $t/\bar{d}$ of 10 and 60 [Figs. 8-9(a1), (a2)]. Small amounts of voids are observed by XCT, and the fracture surfaces are flat with very shallow dimples. In an extreme case, the number of voids is only 11 and f is 4.8e-10% [Fig. 8(a2), Table 3]; this f is much smaller than the reported critical f value at fracture of about 0.1% (Azghandi et al., 2020; Mohamadi Azghandi et al., 2020; Shang et al., 2021; Taylor and Sherry, 2012). It is emphasized that the small f is obtained at relatively large deformation with a far-field true strain (ε_{ff}) of 0.43. Meanwhile, localized necking happens at this deformation state [Fig. 8(a2) and Fig. 5(a2)]. This result argues the well-accepted point that ductile fracture is always induced by voids (Kondori et al., 2018; Taylor and Sherry, 2012; Ueda et al., 2014), and necking accelerates void accumulation (Pineau et al., 2016). Accompanied with the formation of small amounts of voids, a rough free surface with large and localized fluctuation presents; it indicates very heterogeneous deformation.

Another ductile damage type is the void-dominated one [Figs. 8-9(b1), (b2)]. In stainless steels with $t/\bar{d}$ of 10 and 60, large number of voids nucleate and grow during deformation. The maximum f reaches 0.0968% [Fig. 8(b1)] and the fractography is featured with large number of deep dimples. Meanwhile, the free surface is relatively smooth with gentle slopes, manifesting a more uniform deformation than the ones with fewer voids. Changing $t/\bar{d}$ enables the regulation of deformation and damage behaviors. By adjusting $t/\bar{d}$, a moderate f, which manifests a mixed damage mode is obtained in both the tested materials [Figs. 8-9(c1), (c2)]. As revealed by XCT and fractography examination, the mixed damage is featured with a larger

number of small voids and dimples, or a small amount of larger voids and deep dimples. Some flat areas exist in the fracture surface. The above results show that with similar large plastic deformation (ε_{ff} =0.42 ~ 0.47), the damage behaviors of metals transform from a void-suppressed mode to void-dominated one. Terming the scenario with larger amounts of voids as void damage (D_l), and the case with fewer voids as strain localization induced damage (D_l), the study focuses on the micro-mechanism for the transformation of D_l and D_v.

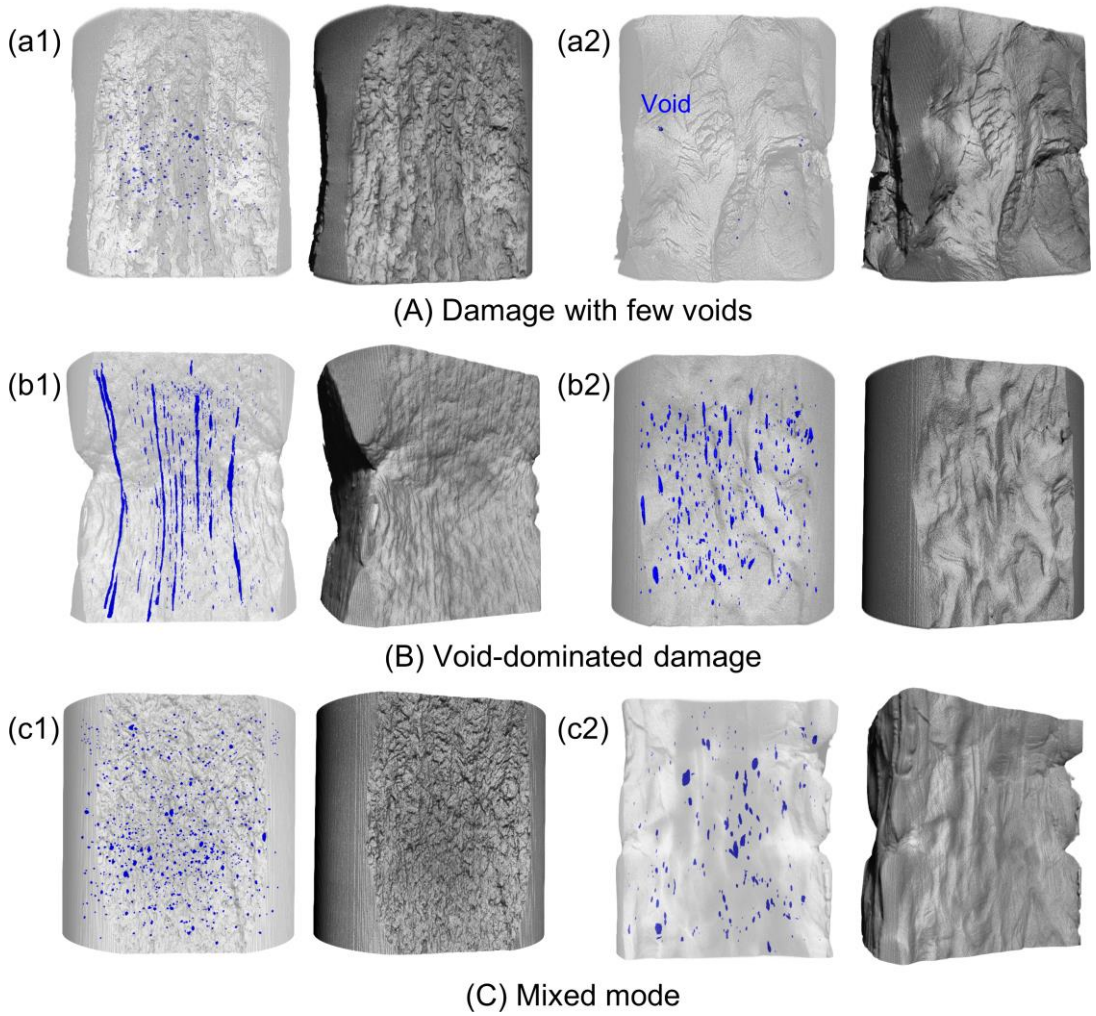

Fig. 8. Ductile damage features of polycrystalline metals. Small amount of voids and heterogeneous deformation show for pure titanium with (a1) $t/\bar{d}$ =60, ε_{ff}=0.47, and (a2), $t/\bar{d}$ =10, ε_{ff}=0.43. Void-dominate damage and smooth surface show for stainless steel 316LN with mono-austenite phase and (b1) $t/\bar{d}$ = 60, ε_{ff} =0.45, and (b2) $t/\bar{d}$ = 10, ε_{ff} =0.45. Moderate f presents for (c1) pure titanium with $t/\bar{d}$ =100, ε_{ff}=0.46, and (c2) 316LN with $t/\bar{d}$ =7.5, ε_{ff}=0.42. (Unit: t is mm, $\bar{d}$ is μm).

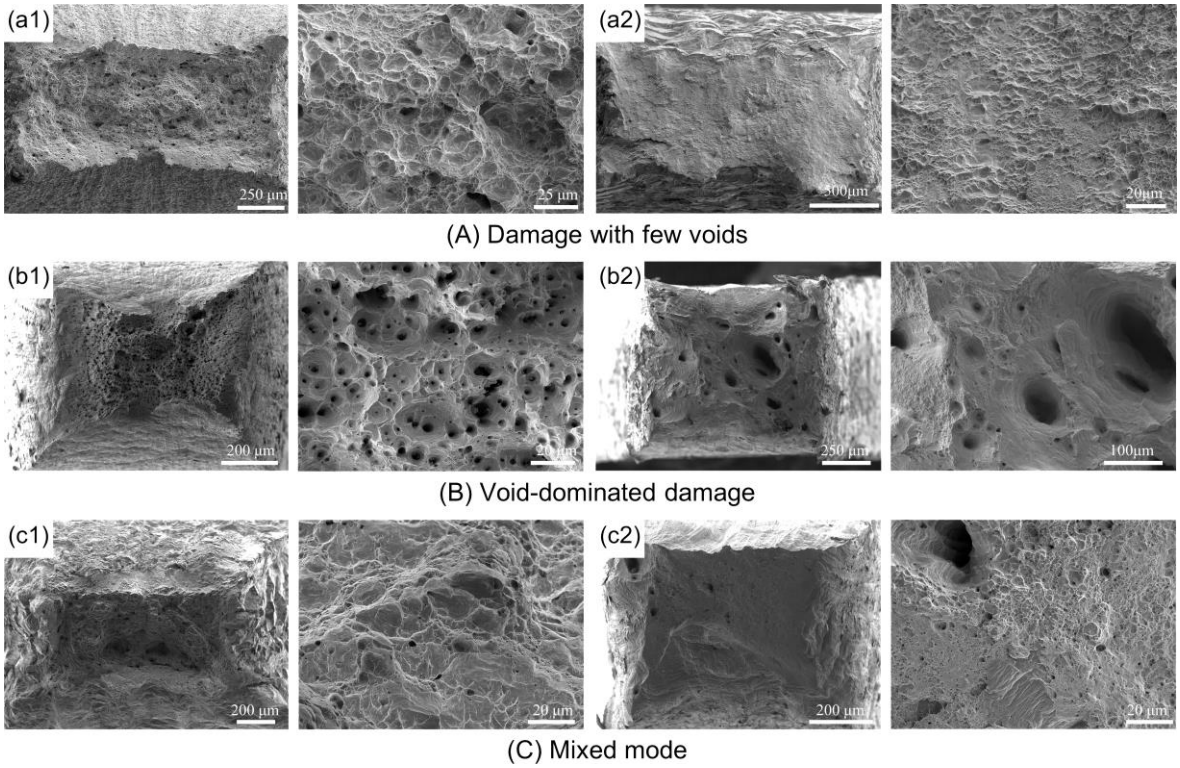

Fig. 9. Morphology of the fracture surface for materials in Fig. 8.

Table 3 Void and strain data for the studied damage scenarios in Fig. 8

Material	Size ratio	Void volume fraction	Average strain at ε_{ff}=0.4
Pure Ti	$t/\bar{d}$=60	0.0210%	0.421
Pure Ti	$t/\bar{d}$=10	4.8e-10%	0.384
316LN	$t/\bar{d}$=60	0.0968%	0.428
316LN	$t/\bar{d}$=10	0.0830%	0.453
Pure Ti	$t/\bar{d}$=100	0.0524%	0.435
316LN	$t/\bar{d}$=7.5	0.0547%	0.451

For void evolution during plastic deformation, we emphasize a nonnegligible feature of volume expansion. It is noted that all the tested materials in the study are initially dense with few voids. The XCT results for parent material with the voxel resolution of 1 μm show no detectable voids [Fig. 3]. Therefore, the observed voids at the pre-fracture condition are outcomes of plastic deformation. The distribution of maximum diameter and volume of voids for a void-dominated damage case [Fig. 8(b2)] is presented in Fig. 10. Larger voids possess dimensions with tens of

microns and volumes of thousands of cubic microns. The quantitative results show that voids can grow by dozens of times during plastic deformation. Many reported data also support a large void volume dilatation (Azghandi et al., 2020; Kondori et al., 2018). Taking void evolution in a magnesium alloy AZ31 for instance, the f is increased from nearly zero to 0.8% when the strain approaches 0.5. Meanwhile, the number of voids is increased to about 300 (Azghandi et al., 2020). The volume dilation of voids has influences on the damage behavior and this factor will be discussed later.

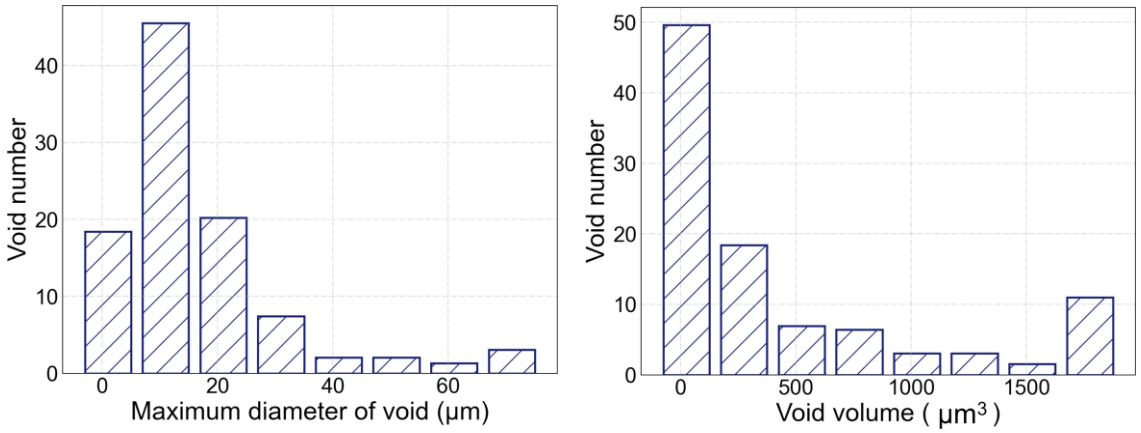

Fig. 10. Distribution of void dimension and volume at the pre-fracture stage for austenite steel with $t/\bar{d}$=10. The data corresponds to a void-dominated damage scenario in Fig. 8(b2).

3.2 Size effect on plastic deformation characteristics and ductile damage

Via adopting $t/\bar{d}$ to represent the size effect, a law that f increases and void contribution becomes dominant with the increase of $t/\bar{d}$ shows for both pure titanium and austenite steel [Table 3]. A direct consideration for the damage behavior variation is that the more void scenarios correspond to larger strains. Classical meso-mechanics fracture theories view void evolution as a mechanical process: local stress/strain concentration drives void nucleation, growth, and coalescence (Gurson, 1977; Rice and Tracey, 1969; Taylor and Sherry, 2012; Ueda et al., 2014). To evaluate the efficiency of this expression in rationalizing the change of damage mode, we adopted CPFEM and DIC to study the strain evolution and distribution. The simulated distributions of equivalent plastic strain ($\bar{\varepsilon}^p$) are present in Fig. 11. From the results, it is obtained that larger strain localization zones occur in the smaller $t/\bar{d}$ scenario [Fig. 11(a),

(c)]. As for the larger $t/\bar{d}$ condition, deformation is characterized by larger number of narrow shear bands and a cross-distribution of large and small deformation zones [Fig. 11(b), (d)].

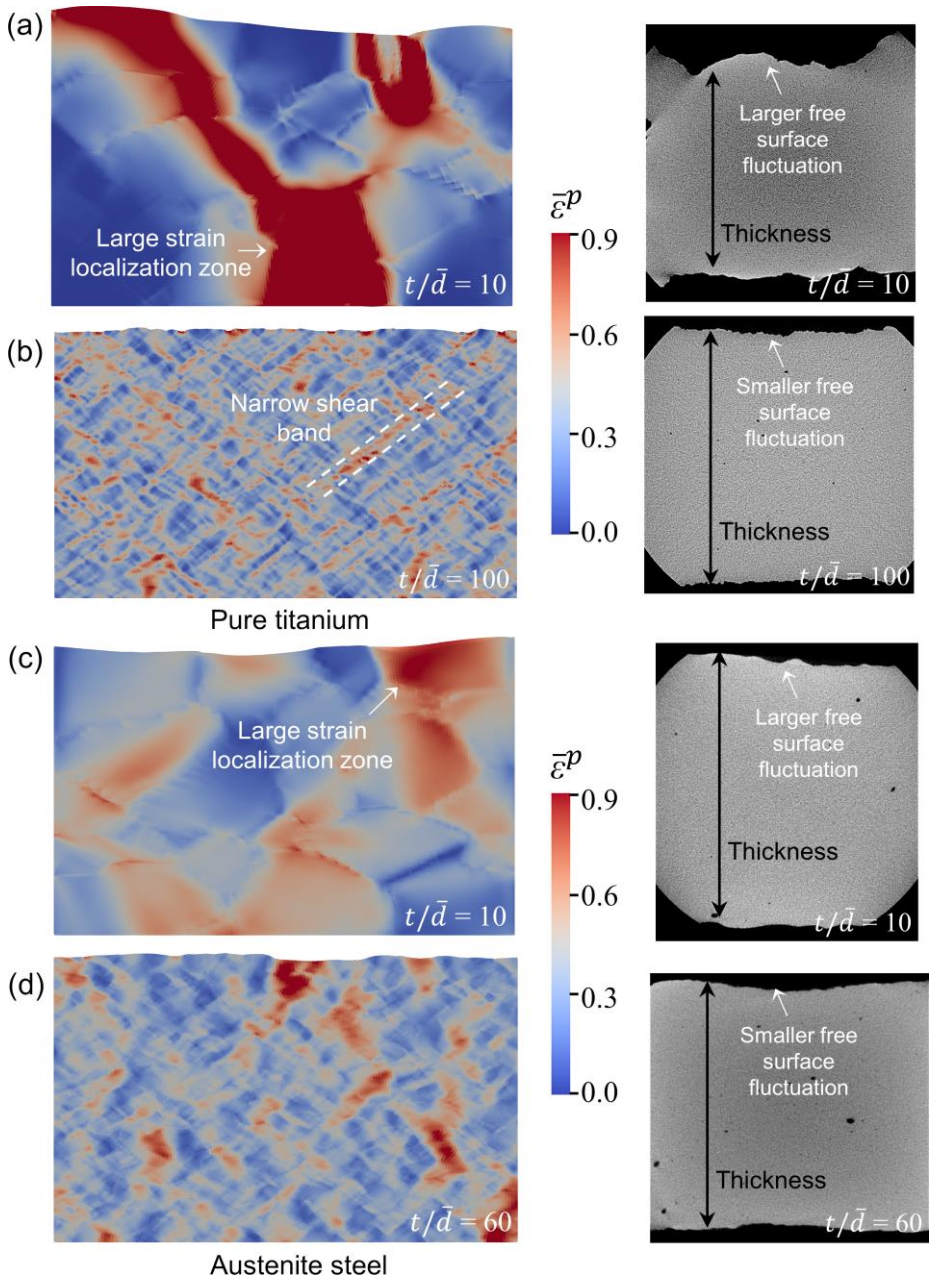

Fig. 11. CPFEM simulated equivalent plastic strain distribution at ε_{ff}=0. 4 and the sample profile obtained by XCT. Results for pure titanium with (a) $t/\bar{d}$ =10, and (b) $t/\bar{d}$ =100. Results for austenite steel with (a) $t/\bar{d}$ =10, and (b) $t/\bar{d}$ = 60.

Rationality of the CPFEM simulation result is validated by the comparisons with the experimental sample profile and strain distribution. From the XCT characterization, a large

free surface fluctuation at the thickness direction appears in the sample with a smaller $t/\bar{d}$ of 10. Regarding the sample with a larger $t/\bar{d}$ of 60 and 100, the free surface features small fluctuations with many small peaks and valleys. The changes of free surface characteristics with $t/\bar{d}$ are well represented by simulations. Since the morphology of free surface is a result of plastic deformation, the comparison of this character provides a corroboration about the simulated deformation characteristics. As for the strain distribution feature, the severe strain concentration in samples with smaller $t/\bar{d}$ is confirmed by the DIC measurements in both the pure titanium and stainless steel. For the larger $t/\bar{d}$ sample, the experiments show a more uniform deformation and many smaller strain localization regions [Fig. 12]. The deformation pattern in terms of the distribution of strain concentration zones represented by experiment and simulation agrees well.

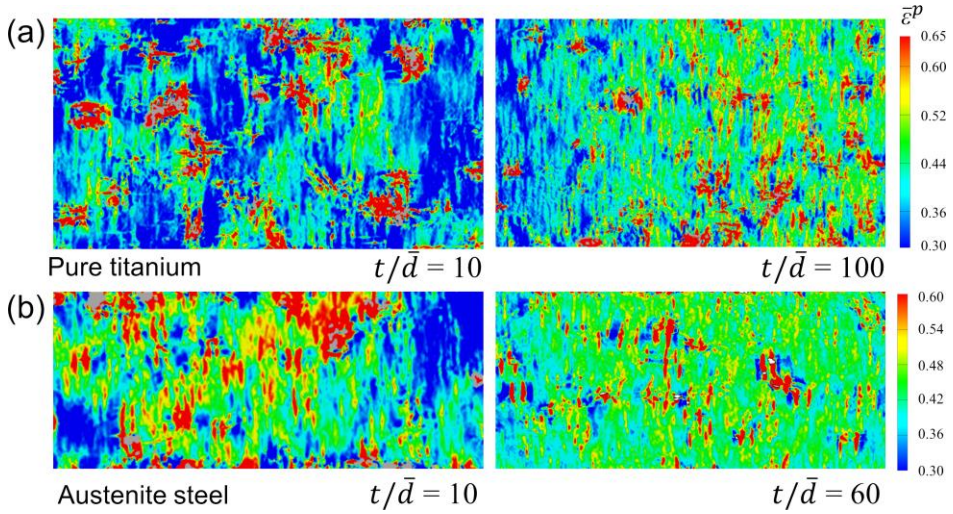

Fig. 12. Equivalent strain measured by the DIC technic. (a) Pure titanium with $t/\bar{d} = 10$ and 100. (b) Austenite steel with $t/\bar{d}$ =10 and 60.

The strain results, together with the void data are analyzed to clarify the relation between damage and deformation. Considering that CPFEM simulations [Fig. 11] give a higher strain resolution than experiment [Fig. 12], the simulated strain data is employed for this discussion. The simulated strain and experimental void data are listed in Table 3. From the results, it is found that the change of $t/\bar{d}$ induces a small change of the average strain while the variation of void behavior is significant. Taking pure titanium with $t/\bar{d}$ =10 and 100 as representative

cases, the two scenarios get average strains of 0.384 and 0.435 at ε_{ff} =0.4, and f of 4.8e-10% and 0.0524%. The condition of fewer voids even gets a larger average strain, manifesting that more voids do not correspond to larger strains. Especially, in an extreme void-suppressed scenario (void no. = 11, f=4.8e-10%) [Fig. 8(a2)], there still exist many areas with strains [Fig. 11(a)] larger than the reported void nucleation strain of 0.1~0.5 (Azghandi et al., 2020; Nemcko and Wilkinson, 2016). Unexpectedly, void is still hard to form. Therefore, apart from strain/stress, additional factors should be involved in uncovering the damage mechanism.

3.3 Damage behavior determined by deformation heterogeneity

Void is a kind of defect in metals; its nucleation and growth are irreversible and energy-consuming. During plastic deformation, new voids nucleate and grow with an obvious volume dilation. The void data in Fig. 10 and reported by previous studies (Azghandi et al., 2020; Kondori et al., 2018; Ueda et al., 2014) demonstrate that plastic deformation can induce the growth of voids by dozens of times. A shortcoming of studying the void behavior only in the mesomechanics framework is the incapability to represent the nucleation and volume expansion. Taking void nucleation as an instance, it describes a phenomenon that an interspace forms in a previous continuous matrix. This process conflicts with the mass conservation law and the continuity hypothesis of mesomechanics. The issue origins from the fact that void evolution is a result of the configuration change of discrete vacancies and dislocations; however, describing the nanoscale discrete behavior is beyond the scope of continuum mechanics. Despite the complexity associated with the micro-mechanism of void behavior, one conclusion is clear: void evolution requires energy.

Throughout plastic deformation, most of the plastic work done by external force is transformed to heat and a small amount is dissipated by the formation of various kinds of defects. (Humphreys and Hatherly, 2012). The generation of grain and subgrain boundaries induced by inhomogeneous deformation and grain rotation provides a primary form of defect aggregation. (Choi and Jin, 2004). Fig. 13 shows the microstructure at fracture surface of pure titanium and

austenite steel with different values of $t/\bar{d}$. As compared to the initial equiaxial grains shown in Fig. 2, it is identified that plenty of grain and subgrain boundaries have been developed during plastic deformation. For pure titanium with a smaller $t/\bar{d}$ of 10, large amounts of grain and subgrain boundaries are developed within individual grains, and the dense boundaries distribute crossly [Fig. 13(a)]. For the larger $t/\bar{d}$ condition, the subdivision of grains is less evident, and the area of grain boundary (GB) is smaller [Fig. 8(b)]. In summary, there are more newly formed boundaries in the $t/\bar{d}$ =10 scenario than the ones for $t/\bar{d}$ =100. Meanwhile, the pure titanium sample with $t/\bar{d}$ =10 gets fewer voids with f of 4.8e-10%, as compared with a larger value of 0.0524% at the $t/\bar{d}$ =100 condition [Table 3]. The phenomenon that more GB boundaries is accompanied by fewer voids is also shown in austenite steels [Fig. 8(c2), (b1), Fig. 13(c), (d)]. The shift of void and grain boundary generation is natural since both mechanisms are energy-consuming.

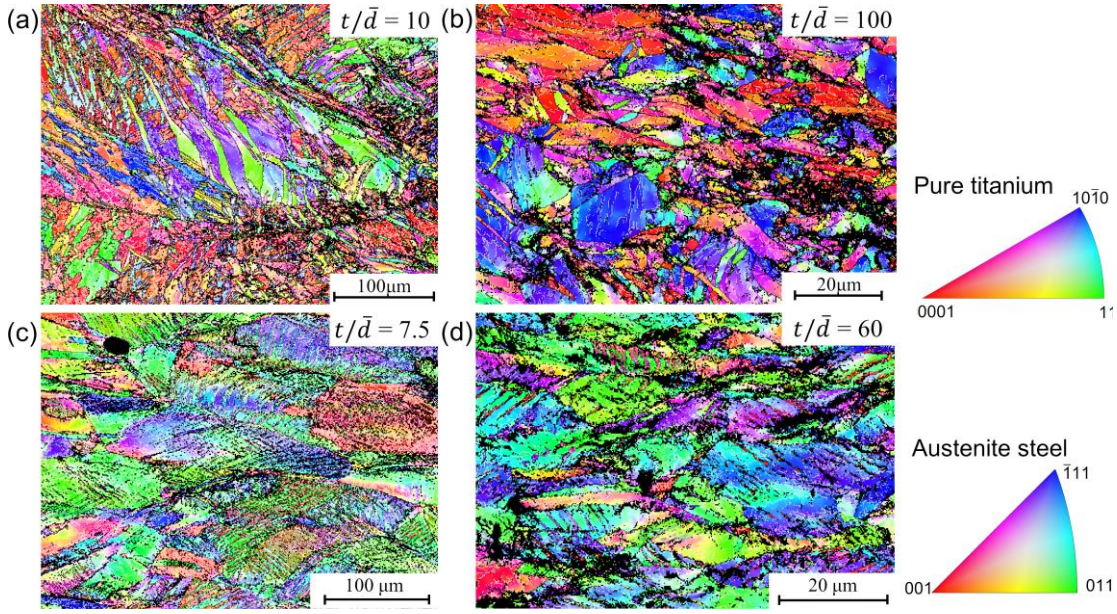

Fig. 13. EBSD results showing grain/subgrain boundary generation. Microstructure at the fracture surface for pure titanium with (a) $t/\bar{d} = 10$ and (b) $t/\bar{d} = 100$. The two cases correspond to the ones with smaller and larger amounts of voids in Fig. 8(a2) and Fig. 8(c1). Austenite steel 316LN with (c) $t/\bar{d}$=7.5 and (d) $t/\bar{d}$=60. The two scenarios correspond to damage conditions in Fig. 8(c2) and Fig. 8(b1). A similar law that more GB boundaries are associated with fewer voids is identified for both materials.

Attention is paid to the deformation characteristics that determine the generation of GBs or voids. CPFEM simulations with high-fidelity microstructures were employed for illustrating this issue [Fig. 14(a)]. In the modeling, each grain involves 18593 elements. Different deformation conditions were constructed by variating grain orientations. Via using Taylor factor as a measure of the deformability of polycrystalline, two representative deformation cases are presented in Fig. 14(b): the RVE with both hard-deformed and easy-deformed grains; and the one with relatively easy-deformed grains. The distribution and evolution of GBs are identified based on the simulated orientation of elements. An element edge is referred as a large angle GB when the misorientation of the adjacent elements becomes larger than 10°; a small angle GB is identified with the ones between 2° and 10°.

Through examining the simulated equivalent plastic strain distribution, it is discovered that a larger strain localization zone is favorable for grain/subgrain boundary formation. The large strain and strain gradient in local regions are responsible for the new boundary development [Fig. 14(c)]. For a relatively uniform deformation scenario, the formation of new GBs only happens adjacent to initial boundaries due to the deformation incompatibility [Fig. 14(d)]. The results of GB evolution confirm that boundary areas grow more rapidly when heterogeneous deformation happens within individual grains [Fig. 14(e)]. Therefore, defects in materials manifest as various kinds of boundaries with the deformation characteristics of greater heterogeneity. Via considering the transition of GB and void generations, voids are thus suppressed in the more non-uniform deformation scenario. Correspondingly, a more homogeneous deformation is associated with more voids. Therefore, the examinations of void feature, deformation pattern, and the microstructure support a conclusion that the increase of deformation heterogeneity leads to a suppression of void generation.

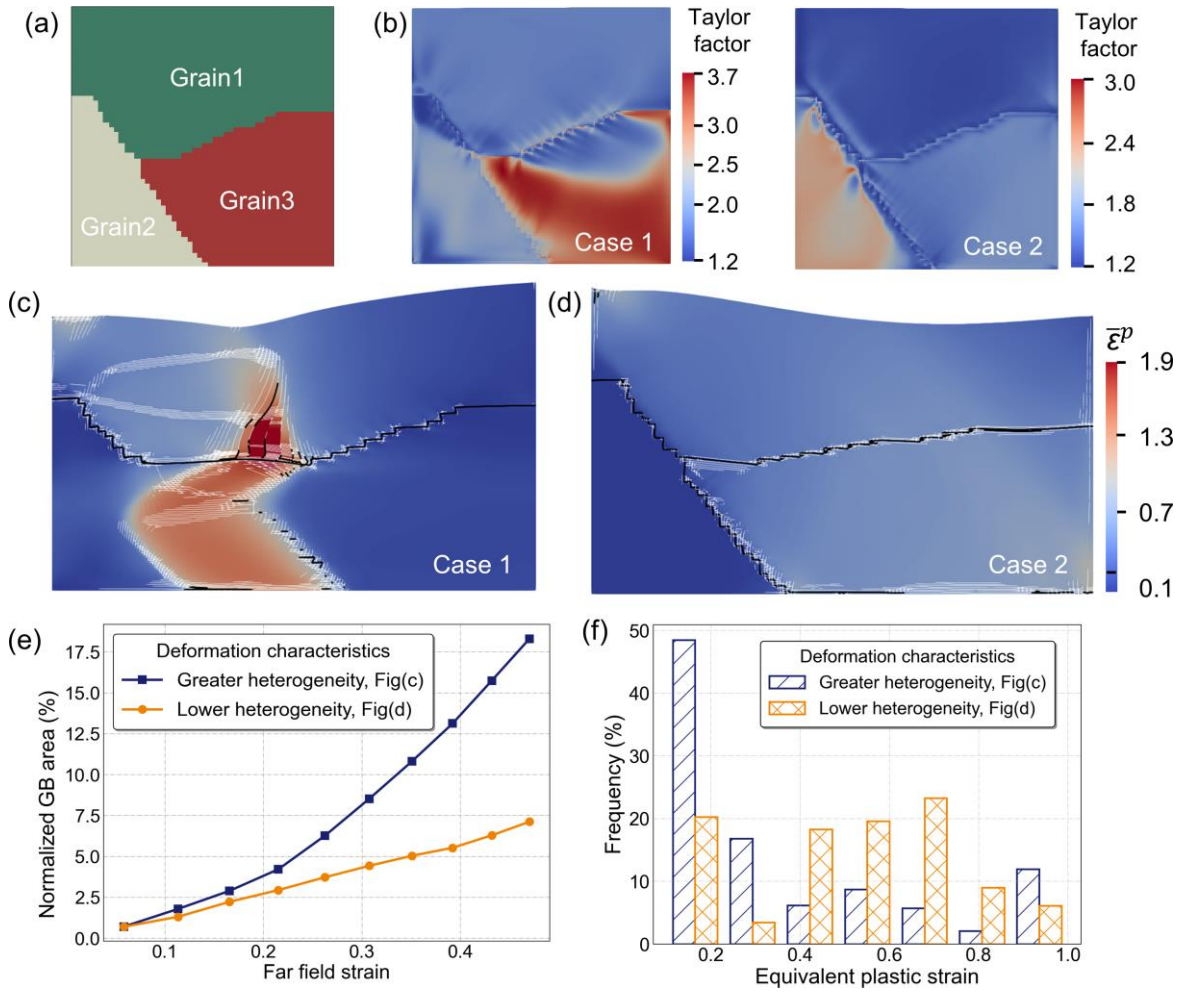

Fig. 14. Relationship between deformation feature and GB generation. (a) RVE with high-fidelity microstructure. (b) Taylor factor distribution of two representative cases. A larger Taylor factor denotes a hard-deformed state. (c)(d) Simulated equivalent plastic strain distribution and boundary areas for scenarios with different deformation uniformities. Black and white lines denote large and small angle GBs. (e) Evolution of GB areas. Normalized GB area is calculated as the percentage of the ratio between boundary length and total length of element edges. (f) Strain distribution for the greater and lower deformation heterogeneity cases.

The correlation between deformation, energy dissipation and micro-defect generation, and ductile damage behavior is thus unraveled. Plastic deformation with greater heterogeneity produces larger continuous strain concentration regions. Complex dislocation structures, grain and subgrain boundaries form in the regions [Fig. 13(a), (c) and Fig. 14(c)]. When the energy

is consumed by new boundary generation, void formation and growth become harder. As the deformation becomes more uniform, the strain localization zone becomes smaller, manifesting as narrow shear bands and the cross-distribution of large and small deformation zones. Without a larger strain concentration zone, boundary development becomes difficult, and voids play a dominant role. This study regards the formulation of new grain GBs as the master factor for ductile damage behavior since it provides a primary form of energy dissipation and storage in metals (Humphreys and Hatherly, 2012). The nucleation and growth of voids are slaves which only occur when the boundary generation is not sufficient. The mechanisms of the two ductile damage modes are summarized in the following:

- Greater deformation heterogeneity → more grain and subgrain boundaries → fewer voids
  The mechanism is termed strain localization induced damage (D_l).
- More uniform deformation → fewer grain and subgrain boundaries → more voids
  The mechanism is termed void damage (D_v).

3.4 Hardening effect on plastic deformation and ductile damage

From the damage feature examinations in Fig. 8, it is discovered that the damage behaviors of the studied two ductile metals show a variation: for a specific $t/\bar{d}$, f of the stainless steel is always larger than that of pure titanium [Fig. 8 and Table 3]. For instance, at $t/\bar{d}$ of 10, f of austenite steel is 0.083% while it is only 4.8e-10% for pure titanium. This study attributes the variation mainly to the difference of the work hardening properties, since hardening greatly affects the extent of deformation localization. A widely known material phenomenon is that the increase of work hardening makes a decrease of local strain concentration. Stainless steel possesses a higher strain hardening rate than pure titanium (Sun et al., 2021; Shang et al., 2020; Wang et al., 2018), and the CPFEM simulation results show that its strain localization is less significant [Figs. 15]. Considering the promotion of GB generation and the suppression of void growth with the enhancement of strain localization, D_l becomes dominant and D_v contributes less to the failure of pure titanium as compared with austenite steel. Quantitative analysis of the deformation pattern is done in accordance with the 3D simulation results. The examination

of strain distribution indicates that more significant deformation localization denotes a more scattered strain distribution with more points possessing strains that deviate largely from the far-field strain value [Fig. 15(d)]. Apart from hardening, other microstructural factors, such as the slip and twinning behaviors also affect the damage modes as they influence the GB formation. However, as the focus of the study is the common laws about ductile fracture, the unique features of specific materials are not given special considerations.

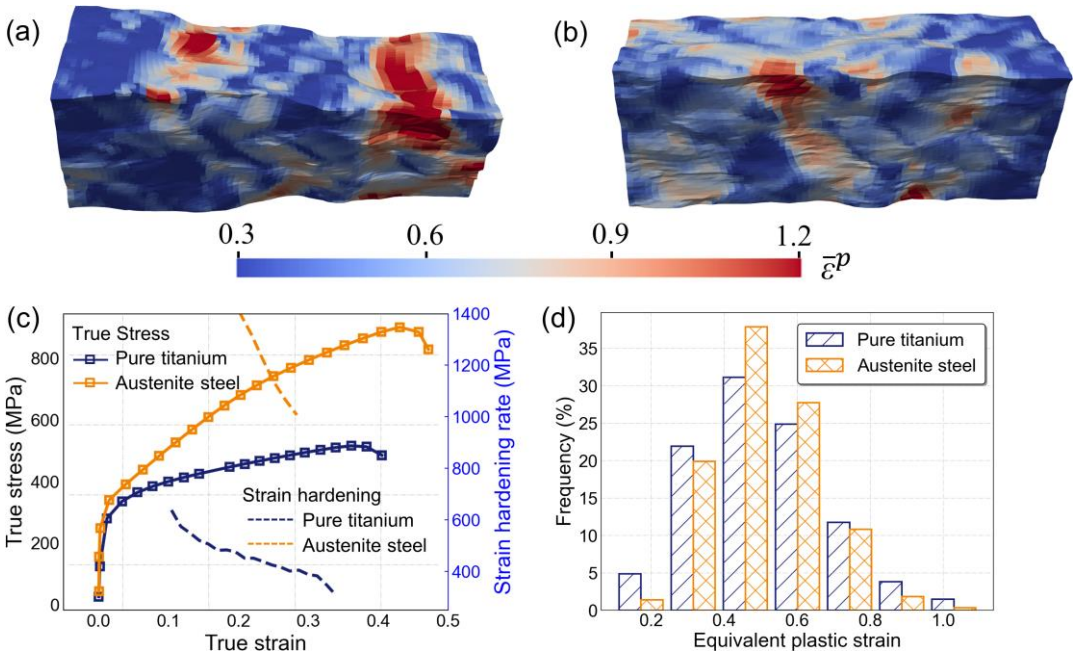

Fig. 15. The influence of hardening on plastic deformation characteristics. 3D CPFEM simulation results of equivalent plastic strain map for $t/\bar{d}$ =10 of (a) pure titanium and (b) austenite steel at ε_{ff}=0.47. (c) The true stress-strain relation and the strain hardening rate. (d) Histogram of strain distribution of pure titanium and austenite steel.

In the analysis of the ductile damage mechanism, size and hardening are influential factors, the generation of GB boundaries and voids are micro-mechanisms, deformation pattern is the determinant factor, and D_l and D_v are the two major damage modes. A schematic illustrating the D_l - D_v transformation is presented in Fig. 16. There are two extended meanings for the proposed damage mechanism: [1] Apart from size and hardening, the factors that affect deformation heterogeneity and the micro-defects accumulation will also influence the damage

behaviors. An instance is provided for torsion. Torsion has a gradient deformation pattern which is favorable for GB generation. Therefore, D_l plays a dominant role in torsion, manifesting as the flat fracture surface with fewer dimples (Faleskog and Barsoum, 2013); [2] There is unclearness associated with the mechanism of D_l. Previous studies describe the process of D_l as coalescence of 'secondary void' at the shear localization band (Bandstra et al., 1998; Besson, 2009; Lou et al., 2014; Roth et al., 2018). Since there is not much experimental evidence illustrating the 'secondary void' mechanism, an issue of 'what is secondary void' arises. From the micro-defect aspect, we consider 'secondary void' refers to the grain/subgrain boundaries. GB boundary is a kind of crystal defect in materials, and a mass amount of this defects inevitably affect the final failure. In view of fewer mesoscale voids and plentiful GB boundaries in the D_l dominated scenario, and the similarity of the flat morphology of GB boundaries and the shear fracture, the plentiful grain/subgrain boundaries formed during plastic deformation are considered as main sources for D_l.

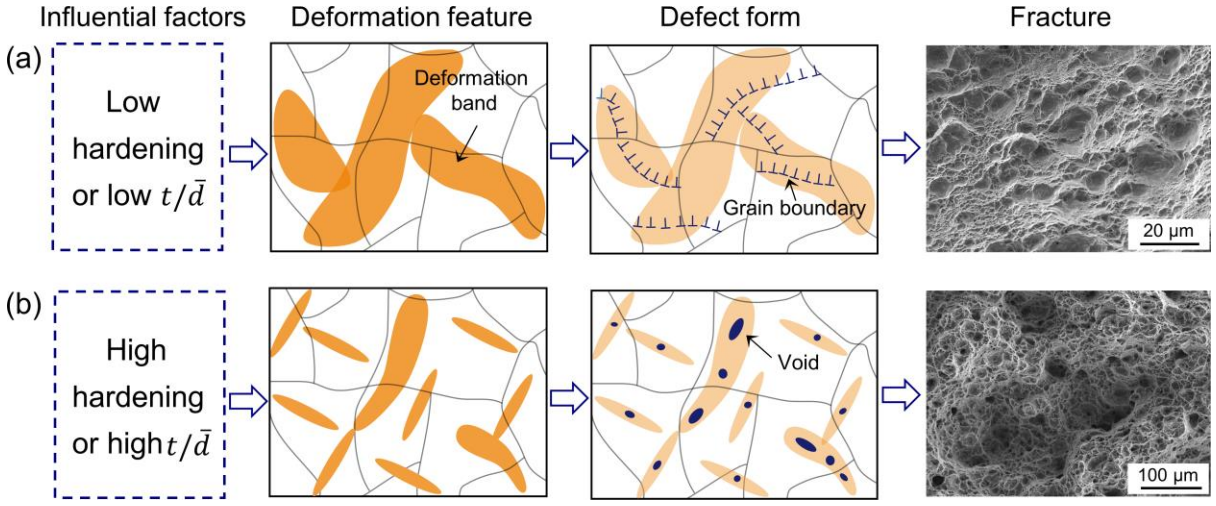

Fig. 16. Schematic diagram illustrating the influential factors and the transformation of damage mechanisms: (a) strain localization induce damage, and (b) void damage.

3.5 Characteristic parameter for the transformation of damage behaviors

The analysis of size and hardening effect on damage behaviors supports a point that as the deformation becomes more heterogeneous, ductile damage mechanism transforms from D_v to D_l. An effort is devoted to defining a representative parameter for this transformation. The

simulation results for grain/subgrain boundary generation [Fig. 14] and the hardening influence of strain localization [Fig. 15] reveal that the greater deformation heterogeneity which triggers GB generation and D_l is featured with a more scattered strain distribution. For a clearer illustration of the relation between non-uniform deformation and strain distribution pattern, we take the ideal homogeneous deformation (strain of each material point equals to the far-field value) as a reference configuration. In this reference case, there is no tendency for strain localization and D_l whatever large the strain is. When strains of some material points deviate from the far-field value, deformation becomes heterogeneous and D_l proceeds. The strong correlation between plastic behavior and the extent of local strain deviation has also been reported for metallic glasses (Wang et al., 2022). Based on the strain distribution characteristics, a parameter representing the extent of deformation heterogeneity is defined in the following:

$$H = \frac{\sum_{n=1}^{n=N}\left(\bar{\varepsilon}_n^p - \varepsilon_{ff}\right)^2}{N} \tag{5}$$

where $\bar{\varepsilon}_n^p$ is the equivalent plastic strain of each material point and ε_{ff} the far-field value; N denotes the number of material points. When calculating H from finite element simulation, $\bar{\varepsilon}_n^p$ and N are related to elements.

H represents the deformation heterogeneity of the whole deformed object. The increase of H manifests a more severe strain localization, a propensity for D_l, and the weaking effect of D_v. The rationality of using H as a representative parameter for the transformation of D_l is D_v is evaluated in terms with the change of deformation and damage performance with $t/\bar{d}$ and hardening. Fig. 17 presents the 3D CPFEM modeling, simulated strain distribution, the free surface fluctuation in thickness direction, and the evolution of H in scenarios of $t/\bar{d}$ =3 and 6. The results, in conjunction with the ones of $t/\bar{d}$=10, are analyzed to illustrate the size effect. It is shown that the RVE with a smaller $t/\bar{d}$ gets an obvious strain localization, a prominent surface fluctuation, and a more rapid growth of H. The simulation results, together with the experimental phenomenon that the void number decreases with a decrease of $t/\bar{d}$ (Furushima

et al., 2014; Xu et al., 2015; Sun et al., 2021; Wang et al., 2018; Shang et al., 2020), demonstrate that void damage is suppressed in the larger H scenario.

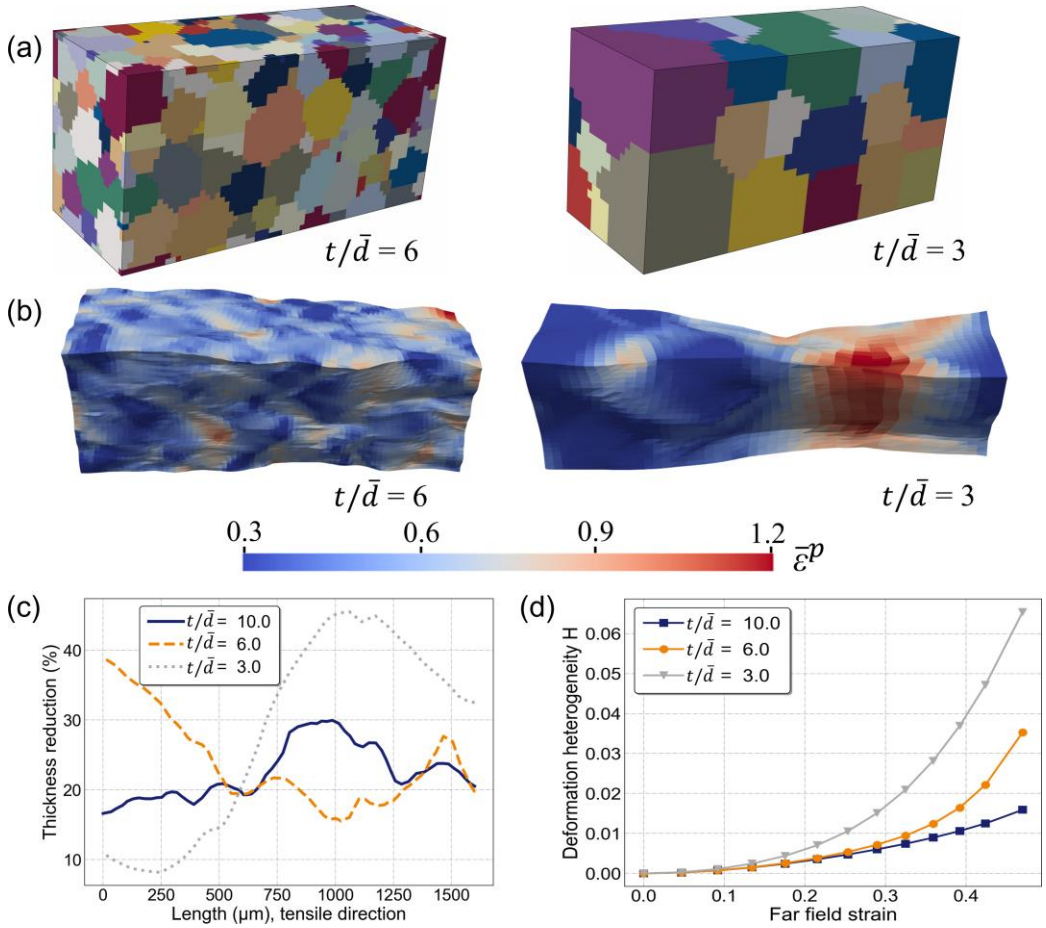

Fig. 17. Adopting H to represent the change of deformation heterogeneity and damage with $t/\bar{d}$: (a) 3D CPFEM modeling for $t/\bar{d}$=6 and $t/\bar{d}$=3. (b) Simulated strain distribution map. (c) Free surface fluctuation represented by thickness reduction along tensile direction. (d) Evolution of H.

Regarding the hardening effect, the deformation heterogeneity and H evolution for low-hardening pure titanium and high-hardening austenite steel at $t/\bar{d}$=10 are examined and analyzed [Fig. 18]. Pure titanium possesses significant local thickness reduction, which indicates severe strain concentration and localized necking [Fig. 18(a)]. While for austenite steel, the free surface fluctuation is relatively smooth. Meanwhile, pure titanium gets a faster growth of H [Fig. 18(b)] and a smaller f of 4.8e-10%, as compared to a larger value of 0.083%

for austenite steel at $t/\bar{d}$=10 [Table 3]. The above quantitative analysis demonstrates a negative correlation between void damage and H, and the efficiency of employing H to characterize the transformation of D_l and D_v.

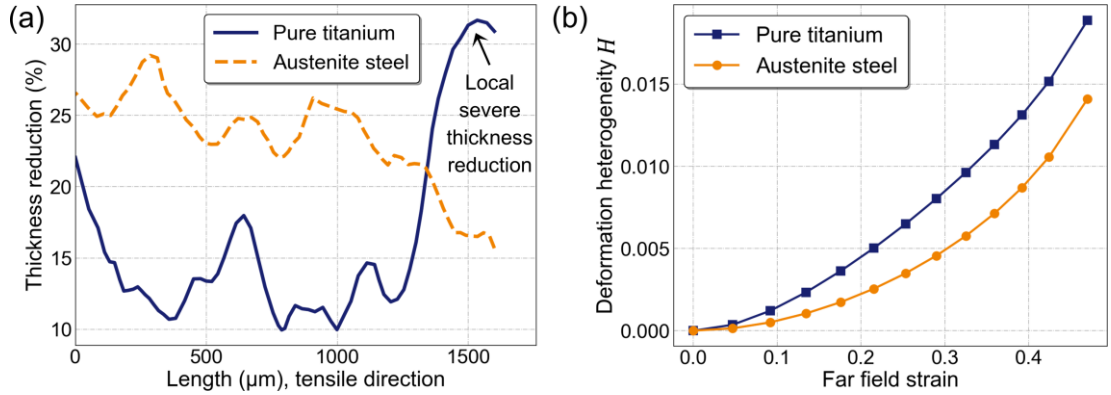

Fig. 18. Adopting H to represent the change of deformation and damage with hardening: (a)(b) Free surface fluctuation represented by thickness reduction along tensile direction, and evolution of H for low-hardening pure titanium and high-hardening austenite steel at condition of $t/\bar{d}$=10.

The understanding about D_l - D_v transformation further determines the modeling methodology. Firstly, we discuss the method employed by previous ductile fracture models. Taking a classical GTN type void model as an instance, it measured damage (D) by f: $D = D_v = f$, and regarded the void-suppressed damage as a factor of f_{shear}. The contribution of f_{shear} was represented by accelerating the growth of f (Nahshon and Hutchinson, 2008; Nielsen and Tvergaard, 2010). However, f_{shear} does not actually corresponds to an increase of void volume, leading to ambiguity about this definition. This issue roots in the fact that the accumulation of f_{shear} is associated with the defect aggregation with the form of GB boundaries instead of voids.

This study replaces the void related parameter f_{shear} by a strain localization related mechanism D_l, and measures D_l with a deformation heterogeneity parameter H. As for D_v, it has been widely studied by meso-mechanic with the stress state (σ_{ij}) and equivalent plastic strain ($\bar{\varepsilon}^p$) determined as key influential factors (Gurson, 1977; Rice and Tracey, 1969; Thomason, 1985;

Tvergaard and Needleman, 1984). This study proves that the increase of deformation heterogeneity leads to a suppression of void accumulation, and the formulation of D_v needs to incorporate H. The expression of $D_v(H)$ provides an important supplement for the traditional ductile damage theory to make it capable of representing the phenomenon that a large plastic deformation (ε_{ff}>0.4) does not induce nucleation and obvious growth of voids [Fig. 8(a1), (a2)]. Damage accumulation is a progressive process which accompanies plastic deformation. When the material undergoes a strain increment, both D_l and D_v increase. A unified methodology to analyze ductile damage is established by accounting for the contributions of the two mechanisms:

$$dD = dD_l(|dH|) + dD_v\left(\sigma_{ij}, d\bar{\varepsilon}^p, |dH|\right) \tag{6}$$

where dD, dD_v, dD_l are the accumulation of total damage, void damage, and strain localization induced damage in a strain increment. The change of deformation heterogeneity is a positive factor, and it is expressed by $|dH|$.

3.6 University and wide applicability of the developed damage paradigm

The transformation of D_l and D_v determined by deformation heterogeneity, and the corresponding characteristics parameter of H constitute a D_l - D_v paradigm. The application scope of the proposed damage paradigm is discussed in accordance with the damage phenomena of a variety of metallic materials. Three-dimensional CPFEM simulation, in conjunction with experimental observations, are employed to clarify this damage issue.

Hardening is a key factor affecting the ductility of metal aggregates. It is widely believed that the increase of hardening delays necking and improves ductility (Wu and Fan, 2020). This common law about the hardening effect is analyzed with the D_l - D_v paradigm by carrying out a series of simulations for various hardening scenarios. The studied cases involve hardening component (n) ranging from 0.15 to 0.46. It covers the properties of most engineering materials. Representative simulation results of strain distribution map, strain-stress relation, and the H evolution are presented in Fig. 19. The results reflect the necking delay phenomenon by

hardening improvement and its manifestation of the decrease of H. From all the simulated data listed in Fig. 20(a), a common law that that the increase of n induces a decrease of H, which indicates a decrease of D_l, is obtained. It coincides with the phenomena that hardening improvement helps relieve local strain localization. Wide applicability of the damage mode transformation descriptor H is validated.

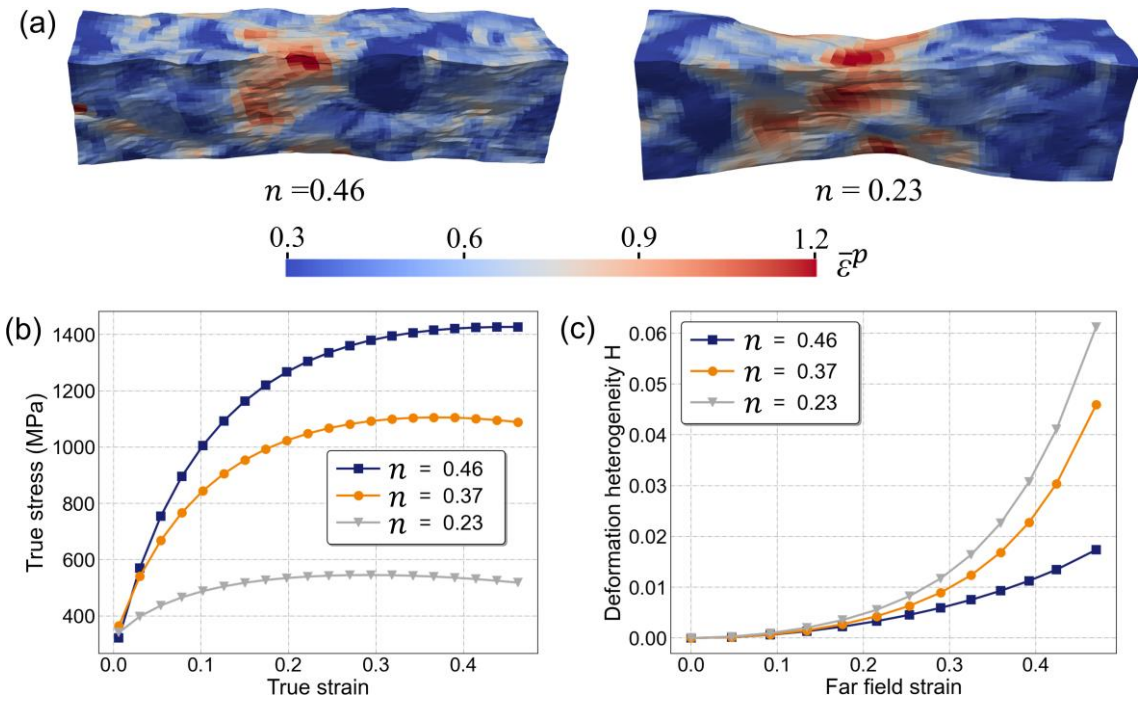

Fig. 19. Representative 3D simulation results for different work hardening conditions: (a) Strain distribution map at ε_{ff}=0.47. (b) True strain and true stress relation. (c) Evolution of H. Hardening component (n) was determined by fitting the stress-strain curve with a Swift constitutive equation.

Elevating hardening has become an efficient strategy in the arena of material design to reconcile the strength-ductility trade-off dilemma (Cheng et al., 2018; Li et al., 2017; Shao et al., 2018; Wu et al., 2017; Wu et al., 2015). In a (FeCoNi) based alloy, the unusual work hardening provided by back stress and forest dislocation helps improve the elongation from 30% to 50% (Yang et al., 2018). Titanium with a heterogeneous lamella structure generates geometrically necessary dislocations in the lamella interfaces, which gives rise to long-range back stress and an elongation improvement from 2.21% to 10.5% (Wu et al., 2015). It is noted

that the ductility improvement via enhancing hardening cannot be well explained if considering ductile damage only from a void viewpoint. Incorporating D_l and D_v into a single framework gives a reasonable interpretation for this material phenomenon: with the increase of hardening, D_l decreases while the change of D_v is small.

The second material phenomenon applied for interpreting the wide applicability of the D_l - D_v paradigm is the coupled influence of size and hardening on ductile damage. Experimental observations of pure titanium, austenite steel [Fig. 8], pure copper and irons (Furukimi et al., 2017; Shang et al., 2020; Xu et al., 2015) show a common law that the number of void increases with the increase of $t/\bar{d}$. Traditional theories rationalize the damage behavior change with $t/\bar{d}$ via considering the variation of void generation ability in different areas: only the internal regions serve as void initiation sites while the free surface is void-free. This explanation has limits in elucidating the variation of size effect in different metals. Pure copper has a high n of 0.4~0.5, and the critical $t/\bar{d}$ for the fracture mode transition is about 5 (Furushima et al., 2014; Xu et al., 2015). This value becomes larger for the low-hardening pure titanium with n about 0.2 (Daming et al., 2017; Sun et al., 2021; Wang et al., 2018): its fracture still has a void-suppressed feature and a small f of 0.021% when $t/\bar{d}$ is increased to 60 [Fig. 8(a1) and Table 3]. This study rationalizes the size effect via incorporating a factor of deformation heterogeneity: the decrease of $t/\bar{d}$ leads to a more heterogeneous deformation, an increase of H and D_l, and a decrease of D_v [Fig. 17]. Since both $t/\bar{d}$ and hardening affect deformation heterogeneity, the D_l - D_v explanation is capable of representing the coupled effect of size and work hardening. As shown in Fig. 20(a), the change of H with n becomes less significant as $t/\bar{d}$ increases.

By assuming a critical value of H (H=0.025 for instance) for the shift of ductile damage mechanisms, the critical point for the D_v dominated damage, D_l dominated one and a mixed mode are discriminated based on the computed results for various n and $t/\bar{d}$ scenarios [Fig.

20]. The scope for different damage mechanisms is determined with a fitted curve from the points. The predicted ductile damage modes are compared with experimental ones for metal crystals involving copper, titanium and tantalum (Boyce et al., 2013; Daming et al., 2017; Furushima et al., 2014; Shang et al., 2020; Wang et al., 2018; Xu et al., 2015), and a good agreement is obtained [Fig. 20(b)]. Although this comparison is rough and elementary, it does reveal the ability of the proposed D_l - D_v methodology to articulate the damage mechanisms of metallic materials with different properties and microstructures. Moreover, it proves the possibility to establish a unified damage quantification platform. With the consideration of more microstructural effects, it is expected that more accurate predictions can be acquired.

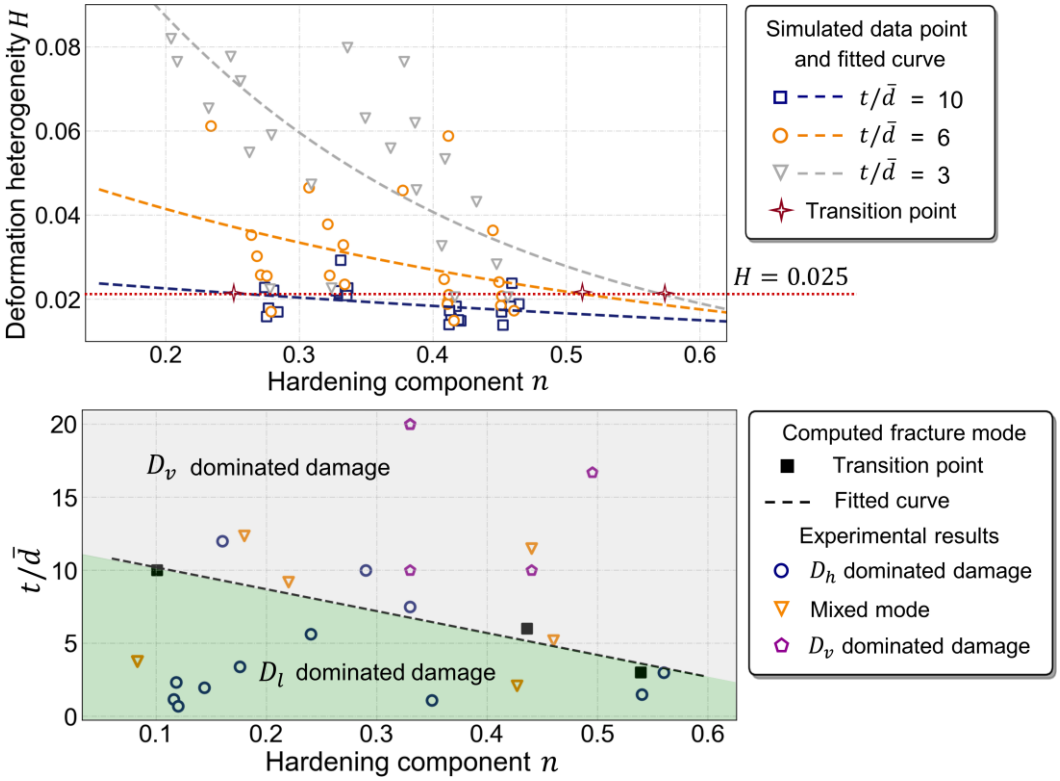

Fig. 20. Coupled influence of hardening and size on the deformation heterogeneity and damage: (a) Relationship between H, n, and $t/\bar{d}$ at ε_{ff}= 0.47. (b) Predictive ability of the D_l - D_v paradigm confirmed by comparison between the predicted damage modes and experimental results. Experimental data involves the damage behavior of pure copper, pure titanium, pure tantalum and stainless steel.

The microstructure factor of the second phase on ductile failure is discussed as this factor affects D_l as well as D_v. Second phases are generally regarded as detrimental factors for ductility as they provide sources for crack nucleation. Examples include Al_2Cu (Taylor and Sherry, 2012) and Mg_2Si (Shen et al., 2013) in aluminum alloys, $Cr_{23}C_6$ or Cr_2N in ferritic steel (Furukimi et al., 2017), reinforcements as TiB in titanium matrix composite (Guo et al., 2012), and Laves phases with low fracture toughness (Ding et al., 2018; Zhu et al., 1999). However, from the aspect of supplying local hardening and delaying necking, second phases can be a positive factor. Especially, when a strongly bonded matrix/phase interface is incorporated (Ding et al., 2018; Yang et al., 2020), the hard phase bears load and sustains shear band formation (Wu et al., 2017), which helps decrease D_l and improve ductility. An example of the delocalization of strain concentration by second phase is shown in Fig. 21. A comprehensive understanding about the relation between ductility and second phase needs to incorporate the decrease of D_l and the increase of D_v. Separating the fundamental role played by D_v and D_l renders physical basis for regulating second phase to improve strength and plasticity simultaneously (Chen et al., 2015).

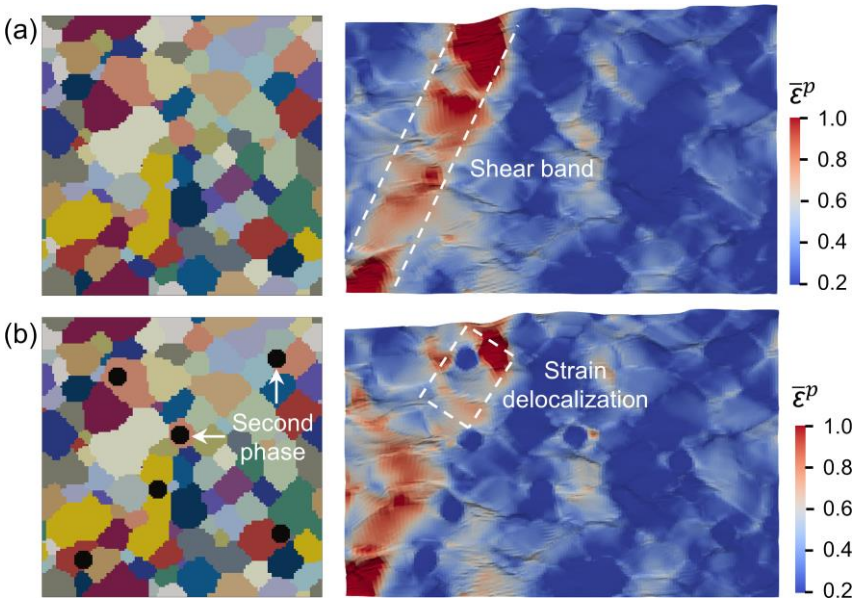

Fig. 21. Second phases provide local hardening to delocalize strain concentration and sustain the formation of deformation band. Modeling and CPFEM simulation results for conditions (a) without second phases, and (b) involving second phases.

The universities and wide applicability of the D_l - D_v paradigm is demonstrated in terms of the influence of hardening, $t/\bar{d}$, and the second phase on the damage performance of a variety of polycrystalline metals. Lacking knowledge about the university of ductile damage mechanism has long been an intractable issue in the material design and forming arena. Material design pursues high ductility by regulating microstructure. However, without a scientific guidance, most of the design works adopt a high cost 'try and error' method. The findings of the study have the potential to accelerate material development via calculating the damage response of various microstructures to determine high performance ones. For the forming issue, developing specific models for different materials requires plenty of experiments. Establishing a unified damage formulation helps reduce the amounts of experiments and simplify the forming technology evaluation procedures, which are urgent needs in industries. For the integrity of the damage platform, explorations about a consistent expression of Eq. (6) are needed for future study.

4. Conclusions

This study explored the transformation mechanism of void damage (D_v) and strain localization induced damage (D_l) induced by the change of grain size, geometrical size, and work hardening property. Pure titanium and austenite steel which are featured with ductile damage were employed for this investigation. Damage characteristics, deformation feature and microstructure were carefully examined to clarify the damage issue. The new findings of this study are listed in the following:

1. Experiments were conducted for representative ductile materials with different grain sizes, sample dimensions, and hardening properties to obtain damage behaviors featured with D_l, D_v and a mixed mode. The results show that with the increase of $t/\bar{d}$ or the increase hardening, the damage mechanism transform from a D_l dominated mode to a D_v dominated one. Through relating damage behaviors to the deformation characteristics, it is found that the deformation with a large strain localization zone is accompanied by a void-suppressed

feature; a more uniform deformation and more voids occur concurrently. The extent of strain localization and deformation heterogeneity is thus identified to be a determining factor for the change of D_l and D_v.

2. The transformation of different ductile damage modes origins from the pattern of energy dissipation. Plastic deformation with a larger strain localization zone is more favorable for grain/subgrain boundary formation. When the energy is consumed by the increase of boundary areas, voids become hard to nucleate and grow. Void formation is more evident when the generation of GB is not sufficient. The microscopic defect forms of GB and voids are the inner controller for D_l and D_v.
3. A characteristic parameter (H) representing the transformation of D_l and D_v is defined based on the strain distribution pattern. An increase of H indicates an increase of deformation heterogeneity, a more dominant role played by D_l, and the corresponding weakened effects of D_v. Incorporating H into the traditional void model helps rationalize the phenomenon that fewer voids generate at large plastic deformation.
4. The proposed D_l - D_v paradigm has universities and wide applicability. The law that greater strain localization is accompanied by fewer voids coincides with the damage performance of a variety of metallic materials. Via conducting simulations for a series of $t/\bar{d}$ and hardening scenarios, a predictive map of ductile damage modes is obtained. The predicted results agree well with experimental ones of different materials, demonstrating the predictive ability and the extensive applicability of the established damage paradigm. The achievements of the study further support the development of a unified damage evaluation platform.

Acknowledgements

This work was supported by the National Natural Science Foundation of China with the projects of Nos. 51825101 and 52001202, and the National Key Research and Development Program (2021YFA1600900).

References:

Azghandi, S.H.M., Weiss, M., Arhatari, B.D., Adrien, J., Maire, E., Barnett, M.R., 2020. A rationale for the influence of grain size on failure of magnesium alloy AZ31: An in situ X-ray microtomography study. Acta Mater. 200, 619-631.

Bai, Y., Wierzbicki, T., 2008. A new model of metal plasticity and fracture with pressure and Lode dependence. Int. J. Plast. 24, 1071-1096.

Bandstra, J.P., Goto, D.M., Koss, D.A., 1998. Ductile failure as a result of a void-sheet instability: experiment and computational modeling. Mater. Sci. Eng. A 249, 46-54.

Besson, J., 2009. Continuum Models of Ductile Fracture: A Review. Inter. J. Damage Mech. 19, 3-52.

Boyce, B.L., Clark, B.G., Lu, P., Carroll, J.D., Weinberger, C.R., 2013. The morphology of tensile failure in tantalum. Metall. Mater. Trans. A 44, 4567-4580.

Boyce, B.L., Kramer, S.L.B., Bosiljevac, T.R., Corona, E., Moore, J.A., Elkhodary, K., Simha, C.H.M., Williams, B.W., Cerrone, A.R., Nonn, A., et al., 2016. The second Sandia Fracture Challenge: predictions of ductile failure under quasi-static and moderate-rate dynamic loading. Int. J. Fract. 198, 5-100.

Boyce, B.L., Kramer, S.L.B., Fang, H.E., Cordova, T.E., Neilsen, M.K., Dion, K., Kaczmarowski, A.K., Karasz, E., Xue, L., Gross, A.J., et al., 2014. The Sandia Fracture Challenge: blind round robin predictions of ductile tearing. Int. J. Fract. 186, 5-68.

Chen, L.Y., Xu, J.Q., Choi, H., Pozuelo, M., Ma, X., Bhowmick, S., Yang, J.M., Mathaudhu, S., Li, X.-C., 2015. Processing and properties of magnesium containing a dense uniform dispersion of nanoparticles. Nature 528, 539-543.

Cheng, Z., Zhou, H., Lu, Q., Gao, H., Lu, L., 2018. Extra strengthening and work hardening in gradient nanotwinned metals. Science 362, eaau1925.

Choi, S.-H., Jin, Y.-S., 2004. Evaluation of stored energy in cold-rolled steels from EBSD data. Mater. Sci. Eng. A 371, 149-159.

Daming, N., Zhen, L., Kaifeng, Z., 2017. Grain size effect of commercial pure titanium foils on mechanical properties, fracture behaviors and constitutive models. J. Mater. Eng. Perform. 26, 1283-1292.

Ding, Z.Y., He, Q.F., Wang, Q., Yang, Y., 2018. Superb strength and high plasticity in laves phase rich eutectic medium-entropy-alloy nanocomposites. Int. J. Plast. 106, 57-72.

Faleskog, J., Barsoum, I., 2013. Tension-torsion fracture experiments-Part I: Experiments and a procedure to evaluate the equivalent plastic strain. Int. J. Solids Struct. 50, 4241-4257.

Fu, M.W., Wang, J.L., 2021. Size effects in multi-scale materials processing and manufacturing. Inter. J. Mach. Tool. Manu. 167, 103755.

Furukimi, O., Kiattisaksri, C., Takeda, Y., Aramaki, M., Oue, S., Munetoh, S., Tanaka, M., 2017. Void nucleation behavior of single-crystal high-purity iron specimens subjected to tensile deformation. Mater. Sci. Eng. A 701, 221-225.

Furushima, T., Tsunezaki, H., Manabe, K.I., Alexsandrov, S., 2014. Ductile fracture and free surface roughening behaviors of pure copper foils for micro/meso-scale forming. Inter. J. Mach. Tool. Manu. 76, 34-48.

Guo, X., Wang, L., Wang, M., Qin, J., Zhang, D., Lu, W., 2012. Effects of degree of

deformation on the microstructure, mechanical properties and texture of hybrid-reinforced titanium matrix composites. Acta Mater. 60, 2656-2667.

Gurson, A.L., 1977. Continuum theory of ductile rupture by void nucleation and growth: Part I-Yield criteria and flow rules for porous ductile media. J. Eng. Mater. Tech. 99, 2-15.

Habib, S.A., Lloyd, J.T., Meredith, C.S., Khan, A.S., Schoenfeld, S.E., 2019. Fracture of an anisotropic rare-earth-containing magnesium alloy (ZEK100) at different stress states and strain rates: Experiments and modeling. Int. J. Plast. 122, 285-318.

Humphreys, F.J., Hatherly, M., 2012. Recrystallization and related annealing phenomena. Elsevier.

Johnson, G.R., Cook, W.H., 1985. Fracture characteristics of three metals subjected to various strains, strain rates, temperatures and pressures. Eng. Fract. Mech. 21, 31-48.

Kadkhodapour, J., Butz, A., Ziaei Rad, S., 2011. Mechanisms of void formation during tensile testing in a commercial, dual-phase steel. Acta Mater. 59, 2575-2588.

Kondori, B., Morgeneyer, T.F., Helfen, L., Benzerga, A.A., 2018. Void growth and coalescence in a magnesium alloy studied by synchrotron radiation laminography. Acta Mater. 155, 80-94.

Sun, L., Xu, Z., Peng, L., Lai, X., 2021. Effect of grain size on the ductile-brittle fracture behavior of commercially pure titanium sheet metals. Mater. Sci. Eng. A 822, 141630.

Li, H., Fu, M.W., Lu, J., Yang, H., 2011. Ductile fracture: Experiments and computations. Int. J. Plast. 27, 147-180.

Li, J., Weng, G.J., Chen, S., Wu, X., 2017. On strain hardening mechanism in gradient nanostructures. Int. J. Plast. 88, 89-107.

Li, Q., Zhang, H., Chen, F., Xu, D., Sui, D., Cui, Z., 2020. Study on the plastic anisotropy of advanced high strength steel sheet: Experiments and microstructure-based crystal plasticity modeling. Int. J. Mech. Sci. 176, 105569.

Lou, Y., Chen, L., Clausmeyer, T., Tekkaya, A.E., Yoon, J.W., 2017. Modeling of ductile fracture from shear to balanced biaxial tension for sheet metals. Int. J. Solids Struct. 112, 169-184.

Lou, Y., Yoon, J.W., Huh, H., 2014. Modeling of shear ductile fracture considering a changeable cut-off value for stress triaxiality. Int. J. Plast. 54, 56-80.

Mohamadi Azghandi, S.H., Weiss, M., Arhatari, B.D., Barnett, M.R., 2020. Grain size and void formation in Mg alloy AZ31. J. Alloy. Compd. 816, 152618.

Nahshon, K., Hutchinson, J.W., 2008. Modification of the Gurson Model for shear failure. Eur. J. Mech. A-Solid. 27, 1-17.

Nemcko, M.J., Wilkinson, D.S., 2016. On the damage and fracture of commercially pure magnesium using x-ray microtomography. Mater. Sci. Eng. A 676, 146-155.

Nielsen, K.L., Tvergaard, V., 2010. Ductile shear failure or plug failure of spot welds modelled by modified Gurson model. Eng. Fract. Mech. 77, 1031-1047.

Noell, P., Carroll, J., Hattar, K., Clark, B., Boyce, B., 2017. Do voids nucleate at grain boundaries during ductile rupture? Acta Mater. 137, 103-114.

Noell, P.J., Sabisch, J.E.C., Medlin, D.L., Boyce, B.L., 2020. Nanoscale conditions for ductile void nucleation in copper: Vacancy condensation and the growth-limited microstructural

state. Acta Mater. 184, 211-224.
Park, K., Nishiyama, M., Nakada, N., Tsuchiyama, T., Takaki, S., 2014. Effect of the martensite distribution on the strain hardening and ductile fracture behaviors in dual-phase steel. Mater. Sci. Eng. A 604, 135-141.
Pedersen, K.O., Westermann, I., Furu, T., Børvik, T., Hopperstad, O.S., 2015. Influence of microstructure on work-hardening and ductile fracture of aluminium alloys. Mater. Design 70, 31-44.
Pineau, A., Benzerga, A.A., Pardoen, T., 2016. Failure of metals I: Brittle and ductile fracture. Acta Mater. 107, 424-483.
Rice, J.R., Tracey, D.M., 1969. On the ductile enlargement of voids in triaxial stress fields∗. J. Mech. Phys. Solids 17, 201-217.
Roters, F., Diehl, M., Shanthraj, P., Eisenlohr, P., Reuber, C., Wong, S.L., Maiti, T., Ebrahimi, A., Hochrainer, T., Fabritius, H.O., et al., 2019. DAMASK-The Düsseldorf Advanced Material Simulation Kit for modeling multi-physics crystal plasticity, thermal, and damage phenomena from the single crystal up to the component scale. Comp. Mater. Sci. 158, 420-478.
Roth, C.C., Morgeneyer, T.F., Cheng, Y., Helfen, L., Mohr, D., 2018. Ductile damage mechanism under shear-dominated loading: In-situ tomography experiments on dual phase steel and localization analysis. Int. J. Plast. 109, 169-192.
Salem, A.A., Kalidindi, S.R., Semiatin, S.L., 2005. Strain hardening due to deformation twinning in α-titanium: Constitutive relations and crystal-plasticity modeling. Acta Mater. 53, 3495-3502.
Selvarajou, B., Joshi, S.P., Benzerga, A.A., 2019. Void growth and coalescence in hexagonal close packed crystals. J. Mech. Phys. Solids 125, 198-224.
Shang, X., Cui, Z., Fu, M., 2017. Dynamic recrystallization based ductile fracture modeling in hot working of metallic materials. Int. J. Plast. 95, 105-122.
Shang, X., Zhang, H., Cui, Z., Fu, M.W., Shao, J., 2020. A multiscale investigation into the effect of grain size on void evolution and ductile fracture: Experiments and crystal plasticity modeling. Int. J. Plast. 125, 133-149.
Shang, X., Zhang, H., Wang, L., Zhu, G., Cui, Z., Fu, M., Zeng, X., 2021. The effect of stress state and strain partition mode on the damage behavior of a Mg-Ca alloy. Int. J. Plast. 144, 103040.
Shao, C.W., Zhang, P., Zhu, Y.K., Zhang, Z.J., Tian, Y.Z., Zhang, Z.F., 2018. Simultaneous improvement of strength and plasticity: Additional work-hardening from gradient microstructure. Acta Mater. 145, 413-428.
Shen, Y., Morgeneyer, T.F., Garnier, J., Allais, L., Helfen, L., Crépin, J., 2013. Three-dimensional quantitative in situ study of crack initiation and propagation in AA6061 aluminum alloy sheets via synchrotron laminography and finite-element simulations. Acta Mater. 61, 2571-2582.
Tancogne-Dejean, T., Roth, C.C., Morgeneyer, T.F., Helfen, L., Mohr, D., 2021. Ductile damage of AA2024-T3 under shear loading: Mechanism analysis through in-situ laminography. Acta Mater. 205, 116556.

Taylor, K.L., Sherry, A.H., 2012. The characterization and interpretation of ductile fracture mechanisms in AL2024-T351 using X-ray and focused ion beam tomography. Acta Mater. 60, 1300-1310.

Thomason, P.F., 1985. A three-dimensional model for ductile fracture by the growth and coalescence of microvoids. Acta Metall. 33, 1087-1095.

Tvergaard, V., 1982. Influence of void nucleation on ductile shear fracture at a free surface. J. Mech. Phys. Solids 30, 399-425.

Tvergaard, V., Needleman, A., 1984. Analysis of the cup-cone fracture in a round tensile bar. Acta Metall. 32, 157-169.

Ueda, T., Helfen, L., Morgeneyer, T.F., 2014. In situ laminography study of three-dimensional individual void shape evolution at crack initiation and comparison with Gurson-Tvergaard–Needleman-type simulations. Acta Mater. 78, 254-270.

Ungár, T., Schafler, E., Hanák, P., Bernstorff, S., Zehetbauer, M., 2007. Vacancy production during plastic deformation in copper determined by in situ X-ray diffraction. Mater. Sci. Eng. A 462, 398-401.

Wang, H., Dmowski, W., Tong, Y., Wang, Z., Yokoyama, Y., Ketkaew, J., Schroers, J., Egami, T., 2022. Nonaffine Strains Control Ductility of Metallic Glasses. Phys. Rev. Lett. 128, 155501.

Wang, S., Niu, L., Chen, C., Pang, Y., Liao, B., Zhong, Z.H., Lu, P., Li, P., Wu, X.D., Coenen, J.W., et al., 2018. Size effects on the tensile properties and deformation mechanism of commercial pure titanium foils. Mater. Sci. Eng. A 730, 244-261.

Wu, G., Chan, K.-C., Zhu, L., Sun, L., Lu, J., 2017. Dual-phase nanostructuring as a route to high-strength magnesium alloys. Nature 545, 80-83.

Wu, H., Fan, G., 2020. An overview of tailoring strain delocalization for strength-ductility synergy. Prog. Mater. Sci. 113.

Wu, X., Yang, M., Yuan, F., Wu, G., Wei, Y., Huang, X., Zhu, Y., 2015. Heterogeneous lamella structure unites ultrafine-grain strength with coarse-grain ductility. PNAS 112, 14501-14505.

Xu, Z.T., Peng, L.F., Fu, M.W., Lai, X.M., 2015. Size effect affected formability of sheet metals in micro/meso scale plastic deformation: Experiment and modeling. Int. J. Plast. 68, 34-54.

Xue, L., 2008. Constitutive modeling of void shearing effect in ductile fracture of porous materials. Eng. Fract. Mech. 75, 3343-3366.

Yang, T., Zhao, Y., Li, W., Yu, C., Luan, J., Lin, D., Fan, L., Jiao, Z., Liu, W., Liu, X., 2020. Ultrahigh-strength and ductile superlattice alloys with nanoscale disordered interfaces. Science 369, 427-432.

Yang, T., Zhao, Y., Tong, Y., Jiao, Z., Wei, J., Cai, J., Han, X., Chen, D., Hu, A., Kai, J., 2018. Multicomponent intermetallic nanoparticles and superb mechanical behaviors of complex alloys. Science 362, 933-937.

Yang, Y., Wang, L., Bieler, T.R., Eisenlohr, P., Crimp, M.A., 2011. Quantitative Atomic Force Microscopy Characterization and Crystal Plasticity Finite Element Modeling of Heterogeneous Deformation in Commercial Purity Titanium. Metall. Mater. Trans. A 42,

636-644.
Zehetbauer M.J., Steiner G., Schafler E., Korznikov A.V., Korznikova E., 2006. Deformation induced vacancies with severe plastic deformation: measurements and modelling. Mater. Sci. Forum 503, 57-64
Zhang, H., Diehl, M., Roters, F., Raabe, D., 2016. A virtual laboratory using high resolution crystal plasticity simulations to determine the initial yield surface for sheet metal forming operations. Int. J. Plast. 80, 111-138.
Zhang, H., Liu, J., Sui, D., Cui, Z., Fu, M.W., 2018. Study of microstructural grain and geometric size effects on plastic heterogeneities at grain-level by using crystal plasticity modeling with high-fidelity representative microstructures. Int. J. Plast. 100, 69-89.
Zhao, Z., Tong, T., Liang, J., Yin, H., Zhao, A., Tang, D., 2014. Microstructure, mechanical properties and fracture behavior of ultra-high strength dual-phase steel. Mater. Sci. Eng. A 618, 182-188.
Zherebtsov, S.V., Dyakonov, G.S., Salem, A.A., Malysheva, S.P., Salishchev, G.A., Semiatin, S.L., 2011. Evolution of grain and subgrain structure during cold rolling of commercial-purity titanium. Mater. Sci. Eng. A 528, 3474-3479.
Zhu, J.H., Liu, C.T., Liaw, P.K., 1999. Phase stability and mechanical behavior of NbCr2-based Laves phases. Intermetallics 7, 1011-1016.